

BRL MR 2796

**BRL**

12

AD

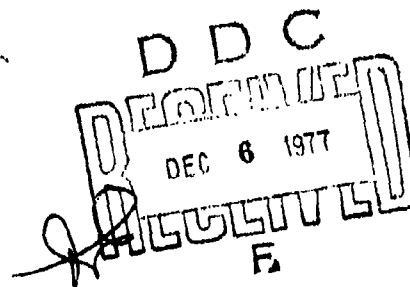
AD A047294

MEMORANDUM REPORT NO. 2796

(Supersedes IMR No. 233)

MISSILE WARHEAD MODELING: COMPUTATIONS  
AND EXPERIMENTS

William W. Predebon  
Walter G. Smothers  
Charles E. Anderson



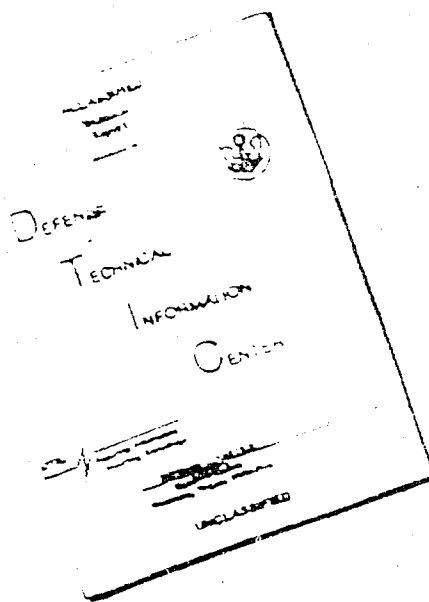
October 1977

Approved for public release; distribution unlimited.

AD No. —  
DDC FILE COPY

USA ARMAMENT RESEARCH AND DEVELOPMENT COMMAND  
USA BALLISTIC RESEARCH LABORATORY  
ABERDEEN PROVING GROUND, MARYLAND

# DISCLAIMER NOTICE



THIS DOCUMENT IS BEST  
QUALITY AVAILABLE. THE COPY  
FURNISHED TO DTIC CONTAINED  
A SIGNIFICANT NUMBER OF  
PAGES WHICH DO NOT  
REPRODUCE LEGIBLY.

REPRODUCED FROM  
BEST AVAILABLE COPY

Destroy this report when it is no longer needed.  
Do not return it to the originator.

Secondary distribution of this report by originating  
or sponsoring activity is prohibited.

Additional copies of this report may be obtained  
from the National Technical Information Service,  
U.S. Department of Commerce, Springfield, Virginia  
22161.

The findings in this report are not to be construed as  
an official Department of the Army position, unless  
so designated by other authorized documents.

*The use of trade names or manufacturers' names in this report  
does not constitute endorsement of any commercial product.*

UNCLASSIFIED

14 BRL-MR-2796

SECURITY CLASSIFICATION OF THIS PAGE (When Data Entered)

REPORT DOCUMENTATION PAGE		READ INSTRUCTIONS BEFORE COMPLETING FORM
1. REPORT NUMBER BRL Memorandum Report No. 2796	2. GOVT ACCESSION NO.	3. RECIPIENT'S CATALOG NUMBER
4. TITLE (and Subtitle) MISSILE WARHEAD MODELING COMPUTATIONS AND EXPERIMENTS	5. TYPE OF REPORT & PERIOD COVERED Final rept.	
6. AUTHOR(s) William W. Predebon, Walter G. Smothers Charles E. Anderson	7. PERFORMING ORG. REPORT NUMBER	
8. PERFORMING ORGANIZATION NAME AND ADDRESS USA Ballistic Research Laboratories Aberdeen Proving Ground, MD 21005	9. CONTRACT OR GRANT NUMBER(s)	
10. CONTROLLING OFFICE NAME AND ADDRESS US Army Materiel Development & Readiness Command 5001 Eisenhower Avenue Alexandria, VA 22333	11. PROGRAM ELEMENT, PROJECT, TASK AREA & WORK UNIT NUMBERS 16 16161102AH43	
12. MONITORING AGENCY NAME & ADDRESS (if different from Controlling Office)	13. REPORT DATE OCT 1977	
	14. NUMBER OF PAGES 1252p	
	15. SECURITY CLASS. (of this report) UNCLASSIFIED	
	16a. DECLASSIFICATION/DOWNGRADING SCHEDULE	
17. DISTRIBUTION STATEMENT (of this Report) Approved for public release; distribution unlimited.		
18. DISTRIBUTION STATEMENT (of the abstract entered in Block 20, if different from Report) DDC DEC 6 1977 REGISTRE F.		
19. SUPPLEMENTARY NOTES Supersedes Interim Memorandum Report No. 233 dated June 1974.		
20. KEY WORDS (Continue on reverse side if necessary and identify by block number) Hemp computations      Warhead Modeling      Radiographic techniques Velocity vector predictions      Explosive testing SAN-D      Liner effects Anti-aircraft warheads      Geometrical variations Preformed fragments      Fragment recovery testing		
21. ABSTRACT (Continue on reverse side if necessary and identify by block number) (k1b) A computational warhead modeling capability has been developed which models the effects of warhead length to diameter ratio, and confinement variation, explosive material and initiation posture, and internal cavity shape and material. These effects are modeled with a time-dependent, two-dimensional, Lagrangian finite-difference computer code, integrally modified to include fragment separation (or fragmentation for continuous warheads) and subsequent explosive gas leakage between fragments.		

DD FORM 1 JAN 73 1473

EDITION OF 1 NOV 65 IS OBSOLETE

150750

UNCLASSIFIED

SECURITY CLASSIFICATION OF THIS PAGE (When Data Entered)

UNCLASSIFIED

SECURITY CLASSIFICATION OF THIS PAGE(When Data Entered)

20. (Cont.) Experimental results of a variety of modeled missile warheads (discrete-fragment warheads) are presented and compared with the computational results. In the experiments the fragment speed and angle distributions with respect to their original position on the warhead are determined through time-sequential, orthogonal flash radiography of the warhead fragment spray in flight, and soft recovery of the fragments after launch. ←

UNCLASSIFIED

SECURITY CLASSIFICATION OF THIS PAGE(When Data Entered)

# TABLE OF CONTENTS

	Page
LIST OF ILLUSTRATIONS . . . . .	5
I. INTRODUCTION . . . . .	9
II. EXPERIMENTAL PROGRAM . . . . .	11
III. COMPUTATIONAL MODELING . . . . .	27
A. Modeling of Discrete Fragments . . . . .	29
B. Fragment Separation and Explosive Gas Leakage . . . . .	31
C. Criterion for Fragment Separation . . . . .	31
IV. COMPARISON BETWEEN COMPUTATIONAL AND EXPERIMENTAL RESULTS .	32
V. CONCLUSIONS AND RECOMMENDATIONS . . . . .	50
ACKNOWLEDGEMENTS. . . . .	51
LIST OF SYMBOLS . . . . .	52
DISTRIBUTION LIST . . . . .	53

AG-155, 10-1-77

NTIS

ED-1

ED-2

ED-3

ED-4

ED-5

ED-6

ED-7

ED-8

ED-9

ED-10

ED-11

ED-12

ED-13

ED-14

ED-15

ED-16

ED-17

ED-18

ED-19

ED-20

ED-21

ED-22

ED-23

ED-24

ED-25

ED-26

ED-27

ED-28

ED-29

ED-30

ED-31

ED-32

ED-33

ED-34

ED-35

ED-36

ED-37

ED-38

ED-39

ED-40

ED-41

ED-42

ED-43

ED-44

ED-45

ED-46

ED-47

ED-48

ED-49

ED-50

ED-51

ED-52

ED-53

ED-54

ED-55

ED-56

ED-57

ED-58

ED-59

ED-60

ED-61

ED-62

ED-63

ED-64

ED-65

ED-66

ED-67

ED-68

ED-69

ED-70

ED-71

ED-72

ED-73

ED-74

ED-75

ED-76

ED-77

ED-78

ED-79

ED-80

ED-81

ED-82

ED-83

ED-84

ED-85

ED-86

ED-87

ED-88

ED-89

ED-90

ED-91

ED-92

ED-93

ED-94

ED-95

ED-96

ED-97

ED-98

ED-99

ED-100

ED-101

ED-102

ED-103

ED-104

ED-105

ED-106

ED-107

ED-108

ED-109

ED-110

ED-111

ED-112

ED-113

ED-114

ED-115

ED-116

ED-117

ED-118

ED-119

ED-120

ED-121

ED-122

ED-123

ED-124

ED-125

ED-126

ED-127

ED-128

ED-129

ED-130

ED-131

ED-132

ED-133

ED-134

ED-135

ED-136

ED-137

ED-138

ED-139

ED-140

ED-141

ED-142

ED-143

ED-144

ED-145

ED-146

ED-147

ED-148

ED-149

ED-150

ED-151

ED-152

ED-153

ED-154

ED-155

ED-156

ED-157

ED-158

ED-159

ED-160

ED-161

ED-162

ED-163

ED-164

ED-165

ED-166

ED-167

ED-168

ED-169

ED-170

ED-171

ED-172

ED-173

ED-174

ED-175

ED-176

ED-177

ED-178

ED-179

ED-180

ED-181

ED-182

ED-183

ED-184

ED-185

ED-186

ED-187

ED-188

ED-189

ED-190

ED-191

ED-192

ED-193

ED-194

ED-195

ED-196

ED-197

ED-198

ED-199

ED-200

ED-201

ED-202

ED-203

ED-204

ED-205

ED-206

ED-207

ED-208

ED-209

ED-210

ED-211

ED-212

ED-213

ED-214

ED-215

ED-216

ED-217

ED-218

ED-219

ED-220

ED-221

ED-222

ED-223

ED-224

ED-225

ED-226

ED-227

ED-228

ED-229

ED-230

ED-231

ED-232

ED-233

ED-234

ED-235

ED-236

ED-237

ED-238

ED-239

ED-240

ED-241

ED-242

ED-243

ED-244

ED-245

ED-246

ED-247

ED-248

ED-249

ED-250

ED-251

ED-252

ED-253

ED-254

ED-255

ED-256

ED-257

ED-258

ED-259

ED-260

ED-261

ED-262

ED-263

ED-264

ED-265

ED-266

ED-267

ED-268

ED-269

ED-270

ED-271

ED-272

ED-273

ED-274

ED-275

ED-276

ED-277

ED-278

ED-279

ED-280

ED-281

ED-282

ED-283

ED-284

ED-285

ED-286

ED-287

ED-288

ED-289

ED-290

ED-291

ED-292

ED-293

ED-294

ED-295

ED-296

ED-297

ED-298

ED-299

ED-300

ED-301

ED-302

ED-303

ED-304

ED-305

ED-306

ED-307

ED-308

ED-309

ED-310

ED-311

ED-312

ED-313

ED-314

ED-315

ED-316

ED-317

ED-318

ED-319

ED-320

ED-321

ED-322

ED-323

ED-324

ED-325

ED-326

ED-327

ED-328

ED-329

ED-330

ED-331

ED-332

ED-333

ED-334

ED-335

ED-336

ED-337

ED-338

ED-339

ED-340

ED-341

ED-342

ED-343

ED-344

ED-345

ED-346

ED-347

ED-348

ED-349

ED-350

ED-351

ED-352

ED-353

ED-354

ED-355

ED-356

ED-357

ED-358

ED-359

ED-360

ED-361

ED-362

ED-363

ED-364

ED-365

ED-366

ED-367

ED-368

ED-369

ED-370

ED-371

ED-372

ED-373

ED-374

ED-375

ED-376

ED-377

ED-378

ED-379

ED-380

ED-381

ED-382

ED-383

ED-384

ED-385

ED-386

ED-387

ED-388

ED-389

ED-390

ED-391

ED-392

ED-393

ED-394

ED-395

ED-396

ED-397

ED-398

ED-399

ED-400

ED-401

ED-402

ED-403

ED-404

ED-405

ED-406

ED-407

ED-408

ED-409

ED-410

ED-411

ED-412

ED-413

ED-414

ED-415

ED-416

ED-417

ED-418

ED-419

ED-420

ED-421

ED-422

ED-423

ED-424

ED-425

ED-426

ED-427

ED-428

ED-429

ED-430

ED-431

ED-432

ED-433

ED-434

ED-435

ED-436

ED-437

ED-438

ED-439

ED-440

ED-441

ED-442

ED-443

ED-444

ED-445

ED-446

ED-447

ED-448

ED-449

ED-450

ED-451

ED-452

ED-453

ED-454

ED-455

ED-456

ED-457

ED-458

ED-459

ED-460

ED-461

ED-462

ED-463

ED-464

ED-465

ED-466

ED-467

ED-468

ED-469

ED-470

ED-471

ED-472

ED-473

ED-474

ED-475

ED-476

ED-477

ED-478

ED-479

ED-480

ED-481

ED-482

ED-483

ED-484

ED-485

ED-486

ED-487

ED-488

ED-489

ED-490

ED-491

ED-492

ED-493

ED-494

ED-495

ED-496

ED-497

ED-498

ED-499

ED-500

ED-501

ED-502

ED-503

ED-504

ED-505

ED-506

ED-507

ED-508

ED-509

ED-510

ED-511

ED-512

ED-513

ED-514

ED-515

ED-516

ED-517

ED-518

ED-519

ED-520

ED-521

ED-522

ED-523

ED-524

ED-525

ED-526

ED-527

ED-528

ED-529

ED-530

ED-531

ED-532

ED-533

ED-534

ED-535

ED-536

ED-537

ED-538

ED-539

ED-540

ED-541

ED-542

ED-543

ED-544

ED-545

ED-546

ED-547

ED-548

ED-549

ED-550

ED-551

ED-552

ED-553

ED-554

ED-555

ED-556

ED-557

ED-558

ED-559

ED-560

ED-561

ED-562

ED-563

ED-564

ED-565

ED-566

ED-567

ED-568

ED-569

ED-570

ED-571

ED-572

ED-573

ED-574

ED-575

ED-576

ED-577

ED-578

ED-579

ED-580

ED-581

ED-582

ED-583

ED-584

ED-585

ED-586

ED-587

ED-588

ED-589

ED-590

ED-591

ED-592

ED-593

ED-594

ED-595

ED-596

ED-597

ED-598

ED-599

ED-600

ED-601

ED-602

ED-603

ED-604

ED-605

ED-606

ED-607

ED-608

ED-609

ED-610

ED-611

ED-612

ED-613

ED-614

ED-615

ED-616

ED-617

ED-618

ED-619

ED-620

ED-621

ED-622

ED-623

ED-624

ED-625

ED-626

ED-627

ED-628

ED-629

ED-630

ED-631

ED-632

ED-633

ED-634

ED-635

ED-636

ED-637

ED-638

ED-639

ED-640

ED-641

ED-642

ED-643

ED-644

ED-645

ED-646

ED-647

ED-648

ED-649

ED-650

ED-651

ED-652

ED-653

ED-654

ED-655

ED-656

ED-657

ED-658

ED-659

ED-660

ED-661

ED-662

ED-663

ED-664

ED-665

ED-666

ED-667

ED-668

ED-669

ED-670

ED-671

ED-672

ED-673

ED-674

ED-675

ED-676

ED-677

ED-678

ED-679

ED-680

ED-681

ED-682

ED-683

ED-684

ED-685

ED-686

ED-687

ED-688

ED-689

ED-690

ED-691

ED-692

ED-693

ED-694

ED-695

ED-696

ED-697

ED-698

ED-699

ED-700

ED-701

ED-702

ED-703

ED-704

ED-705

ED-706

ED-707

ED-708

ED-709

ED-710

ED-711

ED-712

ED-713

ED-714

ED-715

ED-716

ED-717

ED-718

ED-719

ED-720

ED-721

ED-722

ED-723

ED-724

ED-725

ED-726

ED-727

ED-728

ED-729

ED-730

ED-731

ED-732

ED-733

ED-734

ED-735

ED-736

ED-737

ED-738

ED-739

ED-740

ED-741

ED-742

ED-743

ED-744

ED-745

ED-746

ED-747

ED-748

ED-749

ED-750

ED-751

ED-752

ED-753

ED-754

ED-755

ED-756

ED-757

ED-758

ED-759

ED-760

ED-761

ED-762

ED-763

ED-764

ED-765

ED-766

ED-767

ED-768

ED-769

ED-770

ED-771

ED-772

ED-773

ED-774

ED-775

ED-776

ED-777

ED-778

ED-779

ED-780

ED-781

ED-782

ED-783

ED-784

ED-785

ED-786

ED-787

ED-788

ED-789

ED-790

ED-791

ED-792

ED-793

ED-794

ED-795

ED-796

ED-797

ED-798

ED-799

ED-800

ED-801

ED-802

ED-803

ED-804

ED-805

ED-806

ED-807

ED-808

ED-809

ED-810

ED-811

ED-812

ED-813

ED-814

ED-815

ED-816

ED-817

ED-818

ED-819

ED-820

ED-821

ED-822

ED-823

ED-824

ED-825

ED-826

ED-827

ED-828

ED-829

ED-830

ED-831

ED-832

ED-833

ED-834

ED-835

ED-836

ED-837

ED-838

ED-839

ED-840

ED-841

ED-842

ED-843

ED-844

ED-845

ED-846

ED-847

ED-848

ED-849

ED-850

ED-851

ED-852

ED-853

ED-854

ED-855

ED-856

ED-857

ED-858

ED-859

ED-860

ED-861

ED-862

ED-863

ED-864

ED-865

ED-866

ED-867

ED-868

ED-869

ED-870

ED-871

ED-872

ED-873

ED-874

ED-875

ED-876

ED-877

ED-878

ED-879

ED-880

ED-881

ED-882

ED-883

ED-884

ED-885

ED-886

ED-887

ED-888

ED-889

ED-890

ED-891

ED-892

ED-893

ED-894

ED-895

ED-896

ED-897

ED-898

ED-899

ED-900

ED-901

ED-902

ED-903

ED-904

ED-905

ED-906

ED-907

ED-908

ED-909

ED-910

ED-911

ED-912

ED-913

ED-914

ED-915

ED-916

ED-917

ED-918

ED-919

ED-920

ED-921

ED-922

ED-923

ED-924

ED-925

ED-926

ED-927

ED-928

ED-929

ED-930

ED-931

ED-932

ED-933

ED-934

ED-935

ED-936

ED-937

ED-938

ED-939

ED-940

ED-941

ED-942

ED-943

ED-944

ED-945

ED-946

ED-947

ED-948

ED-949

ED-950

ED-951

ED-952

ED-953

ED-954

ED-955

ED-956

ED-957

ED-958

ED-959

ED-960

ED-961

ED-962

ED-963

ED-964

ED-965

ED-966

ED-967

ED-968

ED-969

ED-970

ED-971

ED-972

ED-973

ED-974

ED-975

ED-976

ED-977

ED-978

ED-979

ED-980

ED-981

ED-982

ED-983

ED-984

ED-985

ED-986

ED-987

ED-988

ED-989

ED-990

ED-991

ED-992

ED-993

ED-994

ED-995

ED-996

ED-997

ED-998

ED-999

ED-1000

ED-1001

ED-1002

ED-1003

ED-1004

ED-1005

ED-1006

ED-1007

ED-1008

ED-1009

ED-1010

ED-1011

ED-1012

ED-1013

ED-1014

ED-1015

ED-1016

ED-1017

ED-1018

ED-1019

ED-1020

ED-1021

ED-1022

ED-1023

ED-1024

ED-1025

ED-1026

ED-1027

ED-1028

ED-1029

ED-1030

ED-1031

ED-1032

ED-1033

ED-1034

ED-1035

ED-1036

ED-1037

ED-1038

ED-1039

ED-1040

ED-1041

ED-1042

ED-1043

ED-1044

ED-1045

ED-1046

ED-1047

ED-1048

ED-1049

ED-1050

ED-1051

ED-1052

ED-1053

ED-1054

ED-1055

ED-1056

ED-1057

ED-1058

ED-1059

ED-1060

ED-1061

ED-1062

ED-1063

ED-1064

ED-1065

ED-1066

ED-1067

ED-1068

ED-1069

ED-1070

ED-1071

ED-1072

ED-1073

ED-1074

ED-1075

ED-1076

ED-1077

ED-1078

# LIST OF ILLUSTRATIONS

Figure		Page
1.	Typical Test Configuration . . . . .	12
2.	Test Warhead of $L/D = 2.0$ , with Azimuthal Fragment-Bearing Sector Angle of $22.5^\circ$ . . . . .	13
3.	Typical Radiographic Results for $L/D = 1.0$ Warhead . . . . .	15
4.	Typical Radiographic Results for $L/D = 2.0$ Warhead . . . . .	16
5.	Identification of Fragments in Figure 3 . . . . .	18
6.	Identification of Fragments in Figure 4 . . . . .	19
7.	Radiographic View of Fragment Focusing, $L/D = 2.0$ : Dual End Axial Initiation . . . . .	20
8.	Identification of Fragments in Figure 7 . . . . .	21
9.	Comparison of Round to Round Variation of Warhead Tests . . . . .	22
10.	Variation of "Warhead Performance" with Azimuthal Fragment-Bearing Sector Angle, $L/D = 1.0$ . . . . .	23
11.	Variation of "Warhead Performance" with Azimuthal Fragment-Bearing Sector Angle, $L/D = 2.0$ . . . . .	24
12.	Double-Layered Discrete-Fragment Warheads: Fragment Speed Versus Projection Angle . . . . .	26
13.	Preformed-Fragment Warhead with Al Liner and Al Endplates, $L/D = 2.0$ : Fragment Speed and Projection Angle Distribution . . . . .	28
14.	Comparison of Gurney Velocity and Taylor Angle with HEMP (Fluid Model) Computations and Experimental Data, $L/D = 1.0$ Cylindrical Preformed-Fragment Warhead . . . . .	30
15.	Comparison of Fluid Model Computations and Discrete-Fragment Model Computations with Experimental Data, $L/D = 1.0$ Cylindrical Preformed-Fragment Warhead . . . . .	33

# LIST OF ILLUSTRATIONS (Cont.)

Figure		Page
16.	Comparison of Fluid Model Computations and Discrete-Fragment Model Computations with Experimental Data, $L/D = 2.0$ Cylindrical Preformed-Fragment Warhead . . . . .	34
17.	Comparison of Discrete-Fragment Model Computations with Experimental Data for $L/D = 2.0$ Cylindrical Preformed-Fragment Warhead with Dual End Axial Initiation . . . . .	35
18.	Initiation Postures . . . . .	37
19.	Calculations of Fragment Speed and Projection Angle Distributions for $L/D = 2.0$ Cylindrical Preformed-Fragment Warheads with Dual Axial Point Initiation at $0.10 L$ . . . .	38
20.	Calculations of Fragment Speed and Projection Angle Distributions for $L/D = 2.0$ Cylindrical Preformed-Fragment Warheads with Dual Axial Point Initiation at $0.25 L$ . . . .	39
21.	Calculations of Fragment Speed and Projection Angle Distributions for $L/D = 2.0$ Cylindrical Preformed-Fragment Warheads with Axial Point Initiation at $0.50 L$ . . . . .	40
22.	Calculations of Fragment Speed and Projection Angle Distributions for $L/D = 2.0$ Cylindrical Preformed-Fragment Warheads with Dual End Plane Initiation at $1.00 D$ . . . . .	41
23.	Calculations of Fragment Speed and Projection Angle Distributions for $L/D = 2.0$ Cylindrical Preformed-Fragment Warheads with Dual End Plane Initiation at $0.50 D$ . . . . .	42
24.	Calculations of Fragment Speed and Projection Angle Distributions for $L/D = 2.0$ Cylindrical Preformed-Fragment Warheads with Dual End Peripheral Initiation . . . . .	43
25.	Calculations of Fragment Speed and Projection Angle Distributions for $L/D = 2.0$ Cylindrical Preformed-Fragment Warheads with Dual End Ring Initiation at $0.50 D$ . . . . .	44
26.	Calculations of Fragment Speed and Projection Angle Distributions for $L/D = 2.0$ Cylindrical Preformed-Fragment Warheads with Axial Line Initiation . . . . .	45

# LIST OF ILLUSTRATIONS (Cont.)

Figure		Page
27.	Calculations of Fragment Speed and Projection Angle Distributions for an $L/D = 2.0$ Cylindrical Preformed-Fragment Warhead with Internal Aluminum Cavity Liner and Dual End Axial Initiation . . . . .	46
28.	Calculations of Fragment Speed and Projection Angle Distributions for an $L/D = 2.0$ Cylindrical Preformed-Fragment Warhead with Internal Tungsten Alloy Cavity Liner and Dual End Axial Initiation . . . . .	47
29.	Calculations of Fragment Speed and Projection Angle Distributions for an $L/D = 2.0$ Cylindrical Preformed-Fragment Warhead with an Internal Cavity Modeled as a Vacuum and Dual End Axial Initiation . . . . .	48
30.	Calculations of Fragment Speed and Projection Angle Distributions for an $L/D = 2.0$ Cylindrical Preformed-Fragment Warhead with an Internal Cavity Modeled as Rigid and Dual End Axial Initiation . . . . .	49

## I. INTRODUCTION

Missile warheads are generally quite different in design and construction than warheads used in other military applications, such as artillery shells. This difference mainly is a consequence of the low launch loads experienced by missile warheads. Warhead design in applications where high launch loads are experienced (artillery shells) are usually of the natural fragmentation or controlled fragmentation type. By way of background, natural fragmentation warheads are continuous metal casing warheads with no preselected control sites of failure. Controlled fragmentation warheads, on the other hand, are continuous warheads with preselected control sites or lines of failure. These failure sites are usually arrived at mechanically, metallurgically or explosively. However, missile warheads are generally discrete-fragment warheads and not continuous metal-casing systems. Discrete-fragment warheads are preformed-fragment warheads in which the fragments of the desired shape and mass are placed on a liner (metal or plastic) which encases the high explosive. The warhead is then placed inside a missile casing (skin). These preformed-fragments are attached to the liner and neighboring fragments by an epoxy filler. Due to the very low launch load environment of a missile, this evidently is sufficient for structural integrity.

In the past the main analytical method for predicting fragmentation warhead performance\*, i.e., fragment speed and direction, has been the Gurney<sup>1</sup> and Taylor<sup>2</sup> formulae. These formulae are one-dimensional by assumption and the Gurney formula requires an empirically determined constant. This constant, called the Gurney constant, is obtained experimentally via warhead tests for each different situation. Due to the one-dimensional nature of these formulae, their utility for predicting warhead performance near the ends is questionable. It has been shown<sup>3</sup> that for cases when the flow is essentially one-dimensional, such

*\*Warhead performance as used in this report will mean fragment velocity distribution, which, it can be shown, yields fragment mass distribution.*

<sup>1</sup>Gurney, R. W., "The Initial Velocities of Fragments from Bombs, Shells and Grenades", BRL Report 406, September 1943, AD#36218.

<sup>2</sup>Birkhoff, G., MacDougall, P., Pugh, E. M. and Taylor, G. I., Sir., "Explosives with Lined Cavities", J. Appl. Phys., Vol. 19, p. 563, June 1948.

<sup>3</sup>Karpp, R. R. and Predebon, W. W., "Calculations of Fragment Velocities from Naturally Fragmenting Munitions", BRL Memorandum Report No. 2509, July 1975. (AD #B007377L)

as long artillery projectiles ( $l/D > 2$ ), these formulae are adequate for predicting fragment velocity. However, for cases where the flow is two-dimensional, such as near the warhead ends for any size projectile, and for axisymmetric warheads with length to diameter ratios less than or equal to two, these formulae are inadequate<sup>3</sup>. Lastly, these formulae were initially derived for continuous warheads (i.e., natural fragmentation warheads) and for one specific initiation posture. Consequently, for discrete-fragment warheads, these formulae are not applicable without significant modification and experimental recalibration.

In an effort to find a method to predict warhead performance not only over its midsection but over its entire length including the ends, a time-dependent, two-dimensional, Lagrangian computer code has been applied to naturally fragmenting warheads. In Reference 3, finite-difference calculations of warheads with varying explosive fills and casing materials were compared with experimental results; good agreement was demonstrated. However, the computer code used to obtain the calculations in Reference 3 assumes a continuum. Warheads eventually fragment, and after fragmentation the continuum assumption needs to be modified. A method to model the effects of fragmentation and subsequent explosive gas leakage was presented in Reference 3 as an integral part of the computational scheme.

In this report the earlier work by Karpp and Predebon<sup>3</sup> on natural fragmenting warhead is extended to missile warheads, i.e., discrete-fragment warheads. The objective of the work reported here was to develop a warhead modeling capability to predict the performance of missile warheads in general, as well as warhead designs pertinent to the "Focused-Blast-Fragment" advanced development program.\* Computational modeling was emphasized with limited experimental verification as needed.

In the next section the experimental program is discussed in detail. In Section III the computational modeling is explained. Comparisons between the computational and experimental results are discussed in Section IV. The conclusions and recommendations follow in Section V.

---

\*This work was supported by the BRL, Picatinny Arsenal and AMC, HQ.

## 11. EXPERIMENTAL PROGRAM

Figure 1 is a schematic drawing of part of a typical test set-up used in the warhead test firings for this program. Shown is the warhead on an angled\* wood stand which rests on metal plates on the floor of the second level of the test facility. The two metal plates form a preset aperture through which passes the column of fragments to be radiographed. The lower level of the test facility contains two orthogonal banks (each bank has four flash x-ray tubes) which provide time-sequential, orthogonal radiography.

Due to the funding and time constraints on part of this program, it became obvious at the very beginning that cubical fragments\*\* could not be placed completely around each test warhead and still complete the minimum number of warhead tests planned. Also, from a long term point of view, it is desirable to have a more economical method for testing preformed-fragment warheads. The method used determined the minimum azimuthal-sector angle containing preformed-fragments which adequately represented the situation where the entire cylindrical warhead contained preformed-fragments. All the warheads tested had an overall cylindrical shape. Figure 2 illustrates a test warhead with an azimuthal fragment-bearing sector angle of  $22.5^\circ$  for a typical length to diameter (L/D) ratio of 2.0. In all tests where an azimuthal sector of the warhead contained the preformed-fragments, the remainder of the warhead contained strips (rods) of the same material. The width of the strips was equal to the width of the fragments (for proper radial explosive gas leakage), and the strip lengths were equal to the explosive charge length.

Table I contains all the characteristics of the test warheads by their respective round number. As indicated in Table I, the warhead length to diameter ratio was varied from 1.0 to 2.0. The explosive charge in all cases was Octol (25% TNT, 75% HMX). The fragments were steel (AISI 1018 or 1020) cubes and, in all but one test, were placed directly on the bare explosive charge. This type of configuration was adopted in order to determine with greater accuracy the effect which explosive gas leakage between fragments has on the fragment velocity distribution, particularly for the computational modeling portion of the program.

Figures 3 and 4 illustrate typical radiographic results from L/D = 1.0 and L/D = 2.0 warheads, respectively. Both test warheads were initiated on the axis at the left end. Figures 3 and 4 show the longitudinal and orthogonal views of the fragment distributions in their actual spacial positions at two different times. In each of the test cases the fragments in the radiographed column were premarked for identification and were recovered in Celotex. The spacial location of the recovered premarked

\*The angled wood stand is used to rotate the main fragment distribution into the available radiographic view.

\*\*In all the warhead tests the fragment shape was cubical.

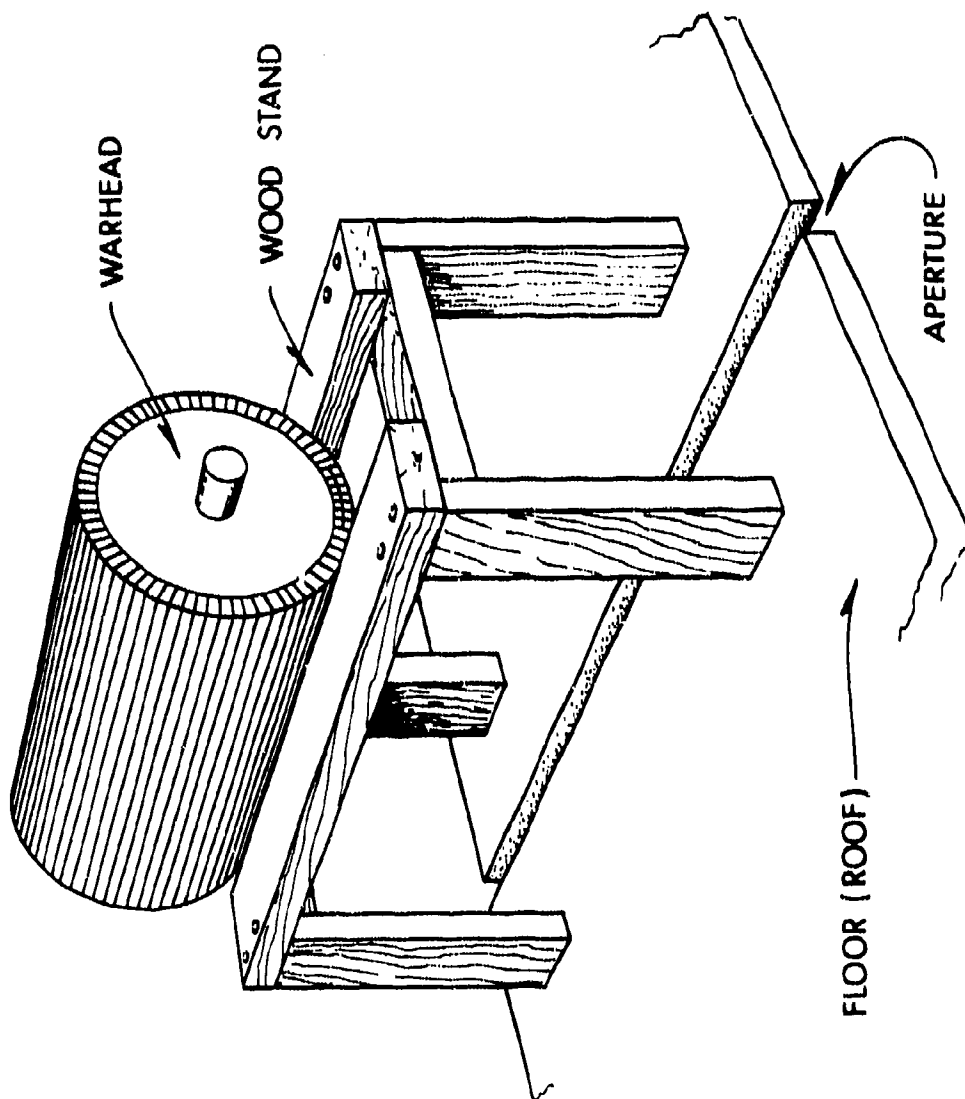


Figure 1. Typical Test Configuration



Figure 2. Test Warhead of  $L/D = 2.0$ , with Azimuthal Fragment-Bearing  
Sector Angle of  $22.5^\circ$

TABLE I. WABILA CHARACTERISTICS AND TEST DATA

Round No.	$\frac{L_{HE}}{P_{HE}}$	$\eta_{HE}$	Fragment Layers	$\alpha_f$	$N_{cc}$	$N_c$	$N_R$	$L_c^1$	$M_c^1$	$M_R^1$	$K_{HE}$	$M_T$	$\bar{C}/M$	$M_{RC}^1$	$M_{RC}^{1,2}$	$P_b/P_0$	$\rho_b$	Initiation <sup>3</sup>
		mm		Degrees				mm	GM	GM	GM	GM		GM	mm		mm	
9237	1	126.04	1	22.5	16	3	47	7.89	3.84	--	2875	3082	.933	3.64	9.58	1.21	140.09	SEA
9310	1	126.04	1	45	16	7	43	7.92	3.87	60.8	2881	3073	.958	3.77	9.37	1.18	140.95	SEA
9264	1	126.04	1	90	16	13	57	7.59	3.84	61.4	2880	3042	.947	3.65	9.75	1.24	140.81	SEA
9242	2	126.04	1	22.5	32	3	47	7.89	3.84	122.7	5743	6136	.936	3.69	9.49	1.20	140.92	SEA
9285	2	126.04	1	45	32	7	43	7.87	3.81	122.0	5743	6099	.942	3.67	9.53	1.21	140.84	SEA
9302	2	126.04	1	45	32	7	43	7.92	3.87	123.0	5729	6155	.931	3.72	9.95	1.26	140.97	SEA
9363	2	126.04	1	90	32	13	36.5	7.95	3.91	124.8	5740	6199	.926	3.80	9.72	1.22	141.07	SEA
9415	2	126.04	1	135	32	19	30.5	7.95	3.92	124.8	5740	6201	.926	3.78	9.79	1.23	141.07	SEA
9323	2	126.04	1	45	32	7	42	7.93	3.89	123.9	5744	6077	.945	3.70	9.55	1.20	140.79	SEA
9317	2	126.04	2 <sup>5</sup>	45	63	13	85	3.96	0.486	62.3	5745	6081	.945	0.438	4.67	1.18	140.80	SEA
9342	2	126.04	2 <sup>6</sup>	45	63	13	84.25	3.96	0.485	63.7	5732	6039	.949	0.464	4.75	1.21	140.70	SEA
9457 <sup>7</sup>	2	125.98	1	90	51	13	57	7.96	3.93	127.8	5608	6315	.889	3.80	9.97	1.25	144.11	SEA

<sup>1</sup>These data represent the average value of the variable.

<sup>2</sup> $M_{RC}$  represents the measured cube dimension in the hoop direction for the recovered cubes.

<sup>3</sup> $R_b/R_0$  is the expansion ratio at fragment separation which is equivalent to  $M_{RC}/L_c$ .

<sup>4</sup>SEA refers to single end axial initiation and HEA refers to dual end axial initiation.

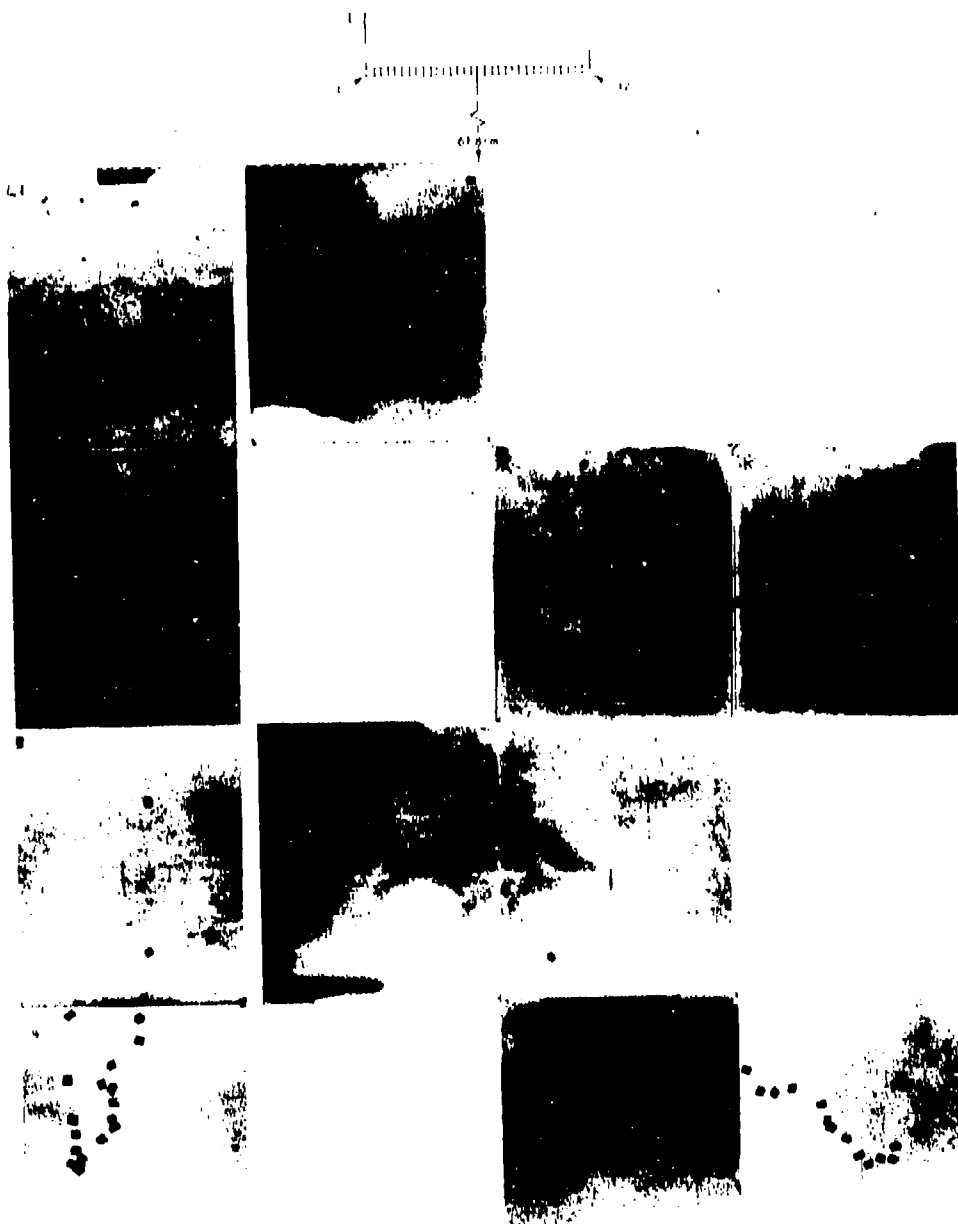
<sup>5</sup>The fragment layers in this test were aligned (See Section II).

<sup>6</sup>The fragment layers in this test were bricked (See Section II).

<sup>7</sup>The liner was 6061-T4 aluminum with a nominal wall thickness of 1.60 mm and total mass of 441 gm. The endplates were 2024-T3 aluminum with a nominal thickness of 6.35 mm and with total masses of 275 gm (detonator endplate) and 270 gm for the other end plate.



Figure 3. Typical Radiographic Results for  $L/D = 1.0$  Warhead



CONCEPTUAL DESIGN

Figure 4. Typical Radiographic Results for  $L/D = 2.0$  Warhead

fragments, in conjunction with the time-sequential, orthogonal radiography of the fragments, permitted development of the results shown in Figures 5 and 6 for the two tests illustrated in Figures 3 and 4. In Figures 5 and 6, each of the fragments in flight are labeled according to their original position on the warhead (shown at the top of the figures). Two different times are shown for both longitudinal and orthogonal views.

To illustrate radiographically the fragment focusing that can be achieved, Figure 7 shows (for two different times) the longitudinal and orthogonal views of an  $L/D = 2.0$  warhead which was initiated simultaneously at both ends on the axis of symmetry. The fragments of Figure 7 are labeled in Figure 8 according to their original position on the warhead. Again two different times are shown for the longitudinal and orthogonal views.

To determine the accuracy of the experimental procedure, a simple error analysis of the measurements was conducted and the round to round variation was quantified. Using a conservative approach to error analysis wherein only maximum differences are considered, for two time-sequential observations of fragments the measurement uncertainty in the fragment speed is less than  $\pm 1\%$  and is less than  $\pm 0.004$  for the tangent of the fragment projection angle. The round to round variation in the warhead tests is shown in Figure 9. Plotted in Figure 9 is the fragment speed and projection angle distributions versus fragment number or relative initial axial position from two tests of nominally identical (See Table I)  $L/D = 2.0$  cylindrical warheads. The round to round variation in fragment speed is  $\pm 3\%$  for two time-sequential observations of the fragments and  $\pm 13\%$  for single time observations of fragments (which occurs for a few fragments at both ends). The overall round to round variation in the tangent of the fragment projection angle is  $\pm 0.02$ . Therefore, it appears that the variations from one round to another (nominally the same) are larger than the measurement uncertainty. Consequently, it was inadvisable to attempt to improve the accuracy of the measurement procedure.

As previously mentioned, the cubical fragments were placed on the warhead in varying azimuthal sector angles, with strips in the remaining azimuthal angle, to determine the minimum azimuthal fragment-bearing sector angle required to approximate the situation in which fragments covered the entire round. Plotted in Figures 10 and 11 are the fragment speed and projection angle distributions for varying azimuthal fragment-bearing sector angles  $\alpha$  for  $L/D = 1.0$  and  $2.0$  warheads, respectively. Since the percent difference between the  $\alpha = 45^\circ$  and  $\alpha = 90^\circ$  cases in Figure 10 is within round to round variation shown in Figure 9, it is felt that a  $45^\circ$  azimuthal fragment-bearing sector angle is adequate for the  $L/D = 1.0$  case. For the  $L/D = 2.0$  case, Figure 11 indicates a large difference between  $\alpha = 22.5^\circ$  and  $\alpha = 45^\circ, 90^\circ$  and  $135^\circ$ . However the differences are much smaller between the  $\alpha = 45^\circ, 90^\circ$  and  $135^\circ$  cases, although the fragment speeds for  $\alpha = 45^\circ$  tend to be greater than or

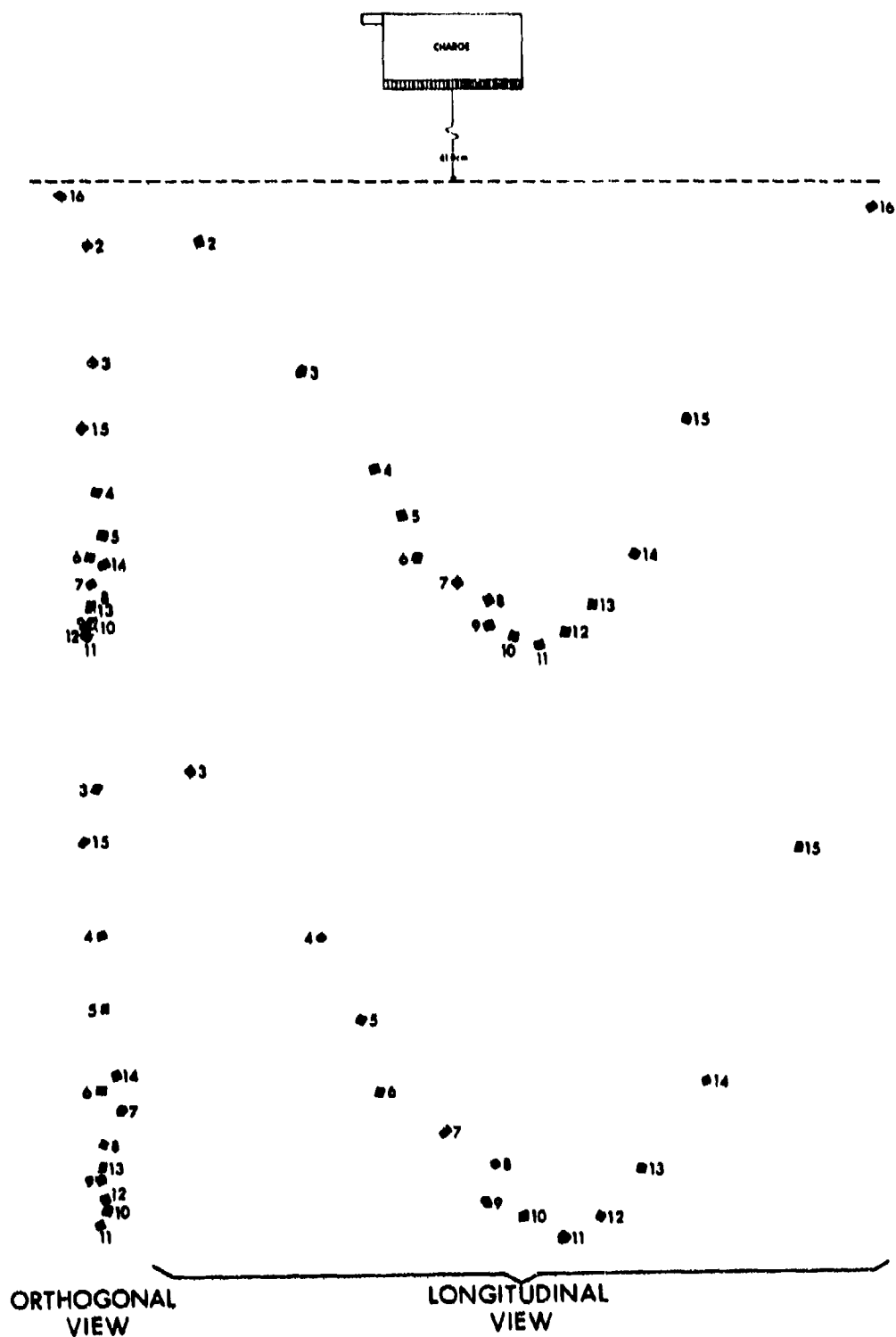


Figure 5. Identification of Fragments in Figure 3

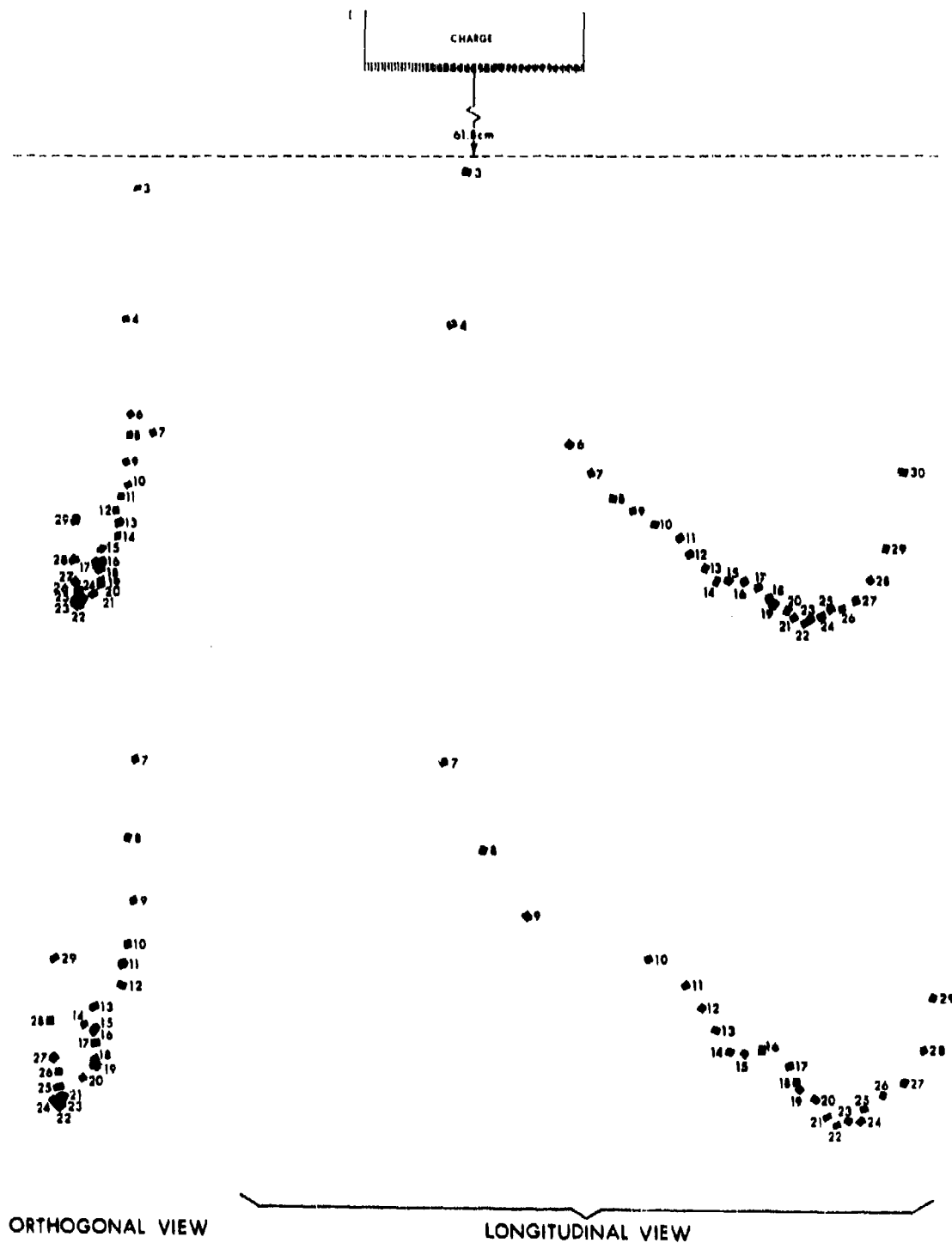


Figure 6. Identification of Fragments in Figure 4



Figure 7. Radiographic View of Fragment Focusing,  
 $L/D = 2.0$ : Dual End Axial Initiation

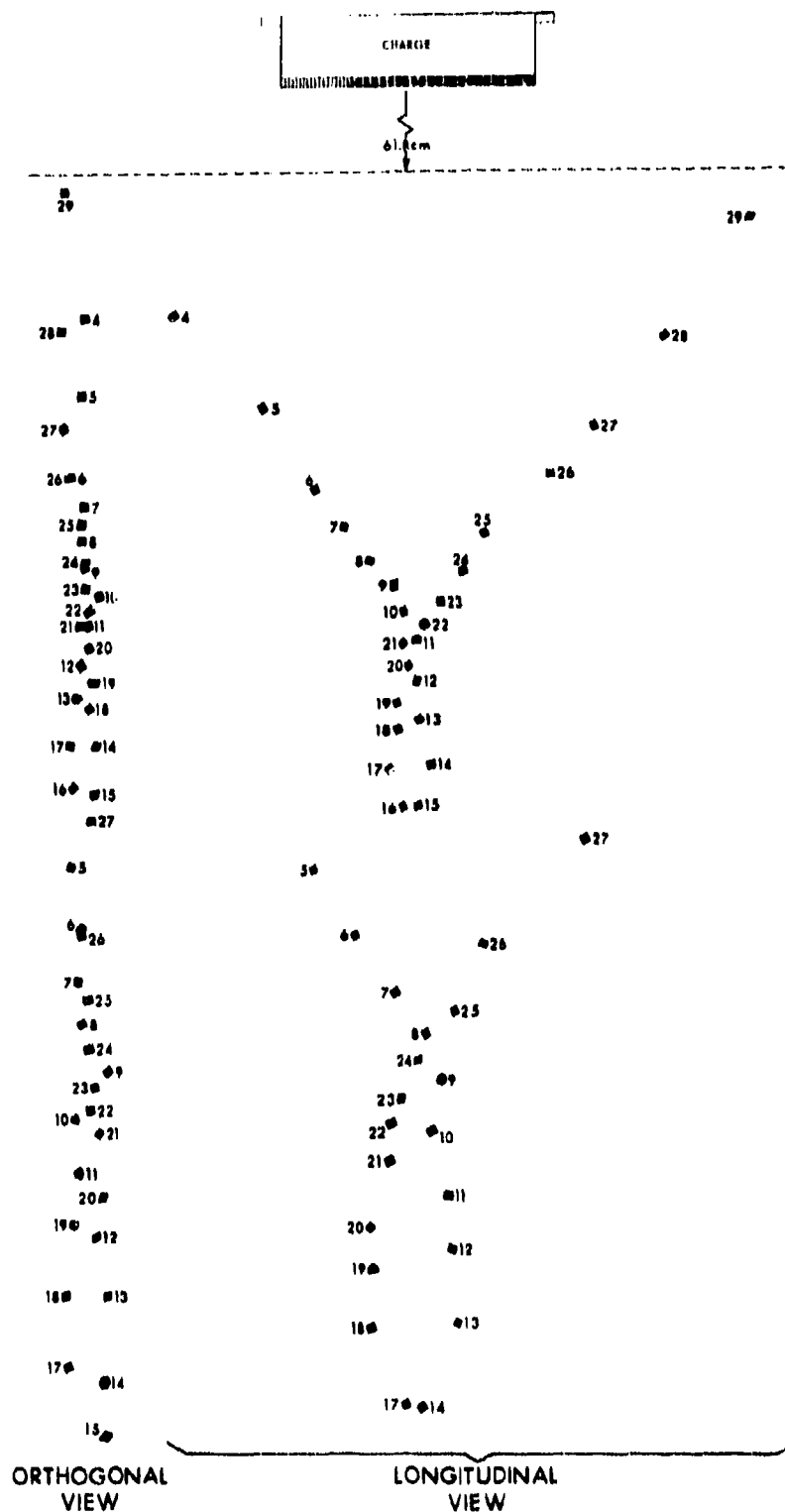


Figure 8. Identification of Fragments in Figure 7

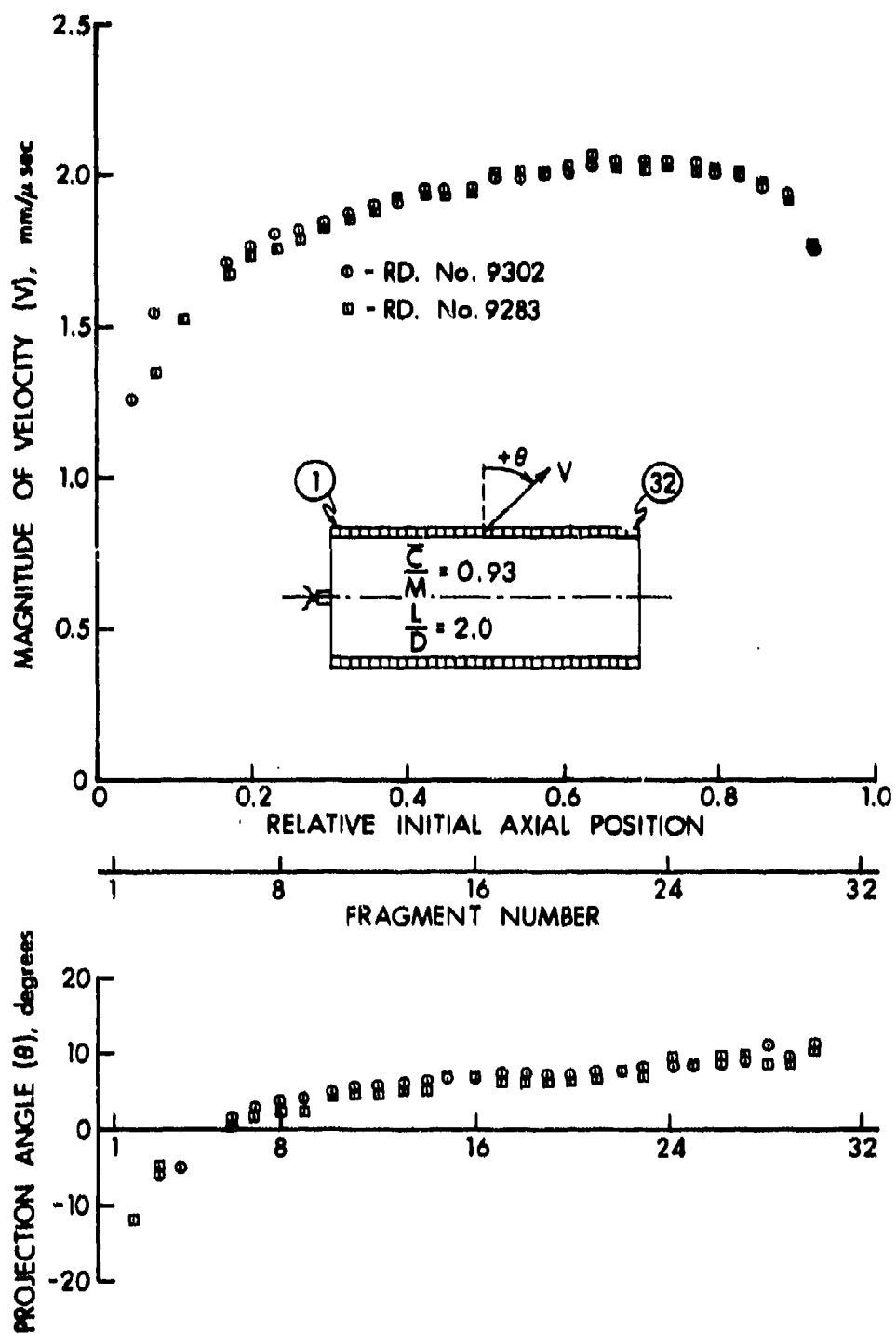


Figure 9. Comparison of Round to Round Variation of Warhead Tests

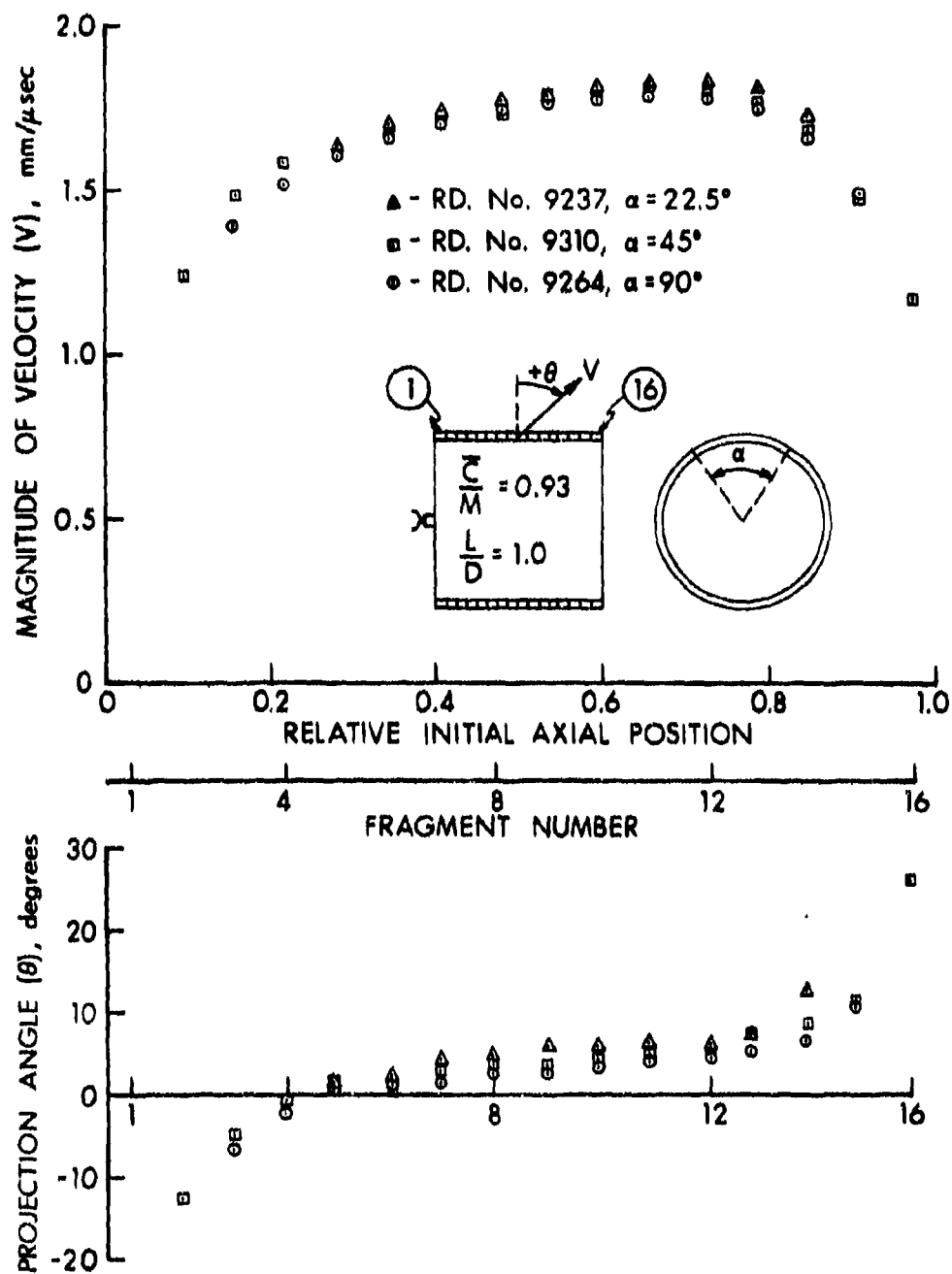


Figure 10. Variation of "Warhead Performance" with Azimuthal Fragment-Bearing Section Angle,  $L/D = 1.0$

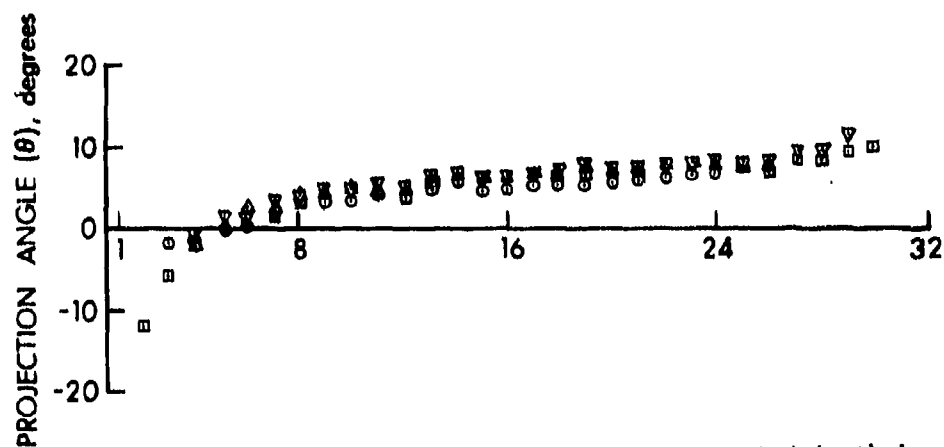
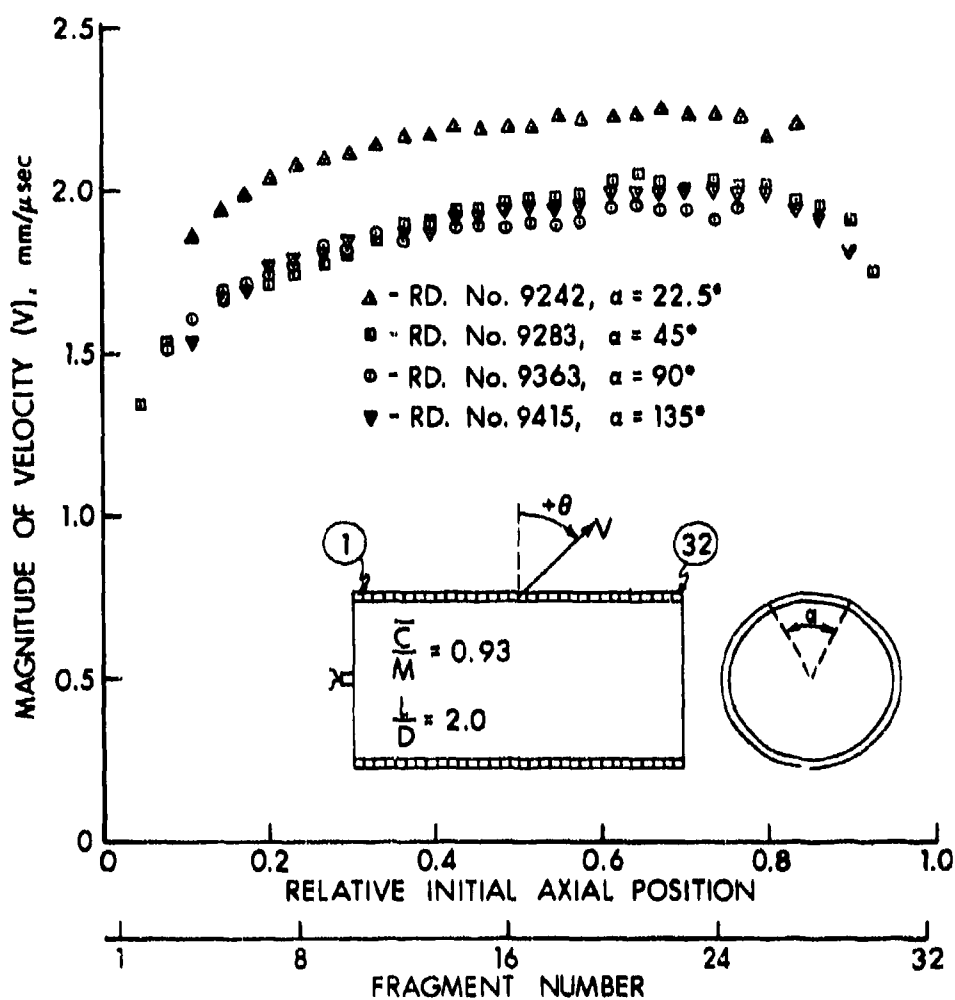


Figure 11. Variation of "Warhead Performance" with Azimuthal Fragment-Bearing Section Angle,  $L/D = 2.0$

equal to  $\alpha = 90^\circ$  or  $\alpha = 135^\circ$ , especially in areas remote from end rarefactions. Mindful of the latter point and the round to round variation shown in Figure 9, the variation in fragment speed between the  $\alpha = 90^\circ$  and  $135^\circ$  is within the round to round variation; whereas the same variation between the  $\alpha = 45^\circ$  and  $90^\circ$  is generally not. In view of the above it is felt that  $\alpha = 90^\circ$  is desirable for the  $L/D = 2.0$  case.

Returning to the  $\alpha = 22.5^\circ$  case in Figure 11, due to the unexpected large differences between it and  $\alpha = 45^\circ$ ,  $90^\circ$  and  $135^\circ$ , particularly near the ends where one would expect the fragment speeds to converge to a common value for most practical  $\alpha$ 's, it is questionable whether these large differences are due to increased confinement for  $\alpha = 22.5^\circ$  or perhaps some uncovered error in the data. An additional test at  $\alpha = 22.5^\circ$  will be required to clarify these questions; however, it was judged that the results of such a test would not significantly change the main thrust and purpose of this study and therefore was not completed at this time.

The experimental results of cases in which computational results were obtained are discussed in Section IV. There are a few test cases for which the computations were not performed during this program and these experimental results will be presented at this time.

The modeling of multi-fragment layering is immensely complicated due to the many combinations of layer patterns that can be placed on the warhead. In order to bracket the effects of the simplest multi-fragment layering case, i.e., two layers of fragments, two double-layered discrete-fragment warheads were fired. The fragment layers were aligned with respect to each other for the first warhead; the other warhead had the fragments bricked (that is, the fragments on the top layer were displaced by a distance equal to half of a cube side relative to the fragments on the bottom layer). In Figure 12 are plotted the results of the aligned and bricked double-layered warheads. In order to compare these results to the single layered test, the charge mass to metal mass (C/M), the type of explosive, explosive initiation and explosive dimensions were kept the same as the single layered  $L/D = 2.0$  case (shown in Figure 16). Further, the fragment shape and fragment material were kept the same. These constraints thus imposed that the double-layered fragment masses be  $1/8$  the single layered masses. Due to the resulting lower cube masses (0.486 gm), and therefore much smaller dimensions, the previously used cube numbering system was not effective in identifying the cubes with respect to their original position on the warhead. When the cubes were recovered they had generally collided with each other during flight and the punched numbers on each fragment were unidentifiable. Consequently the fragment speed is plotted with respect to its projection angle in Figure 12 rather than its initial position on the warhead.

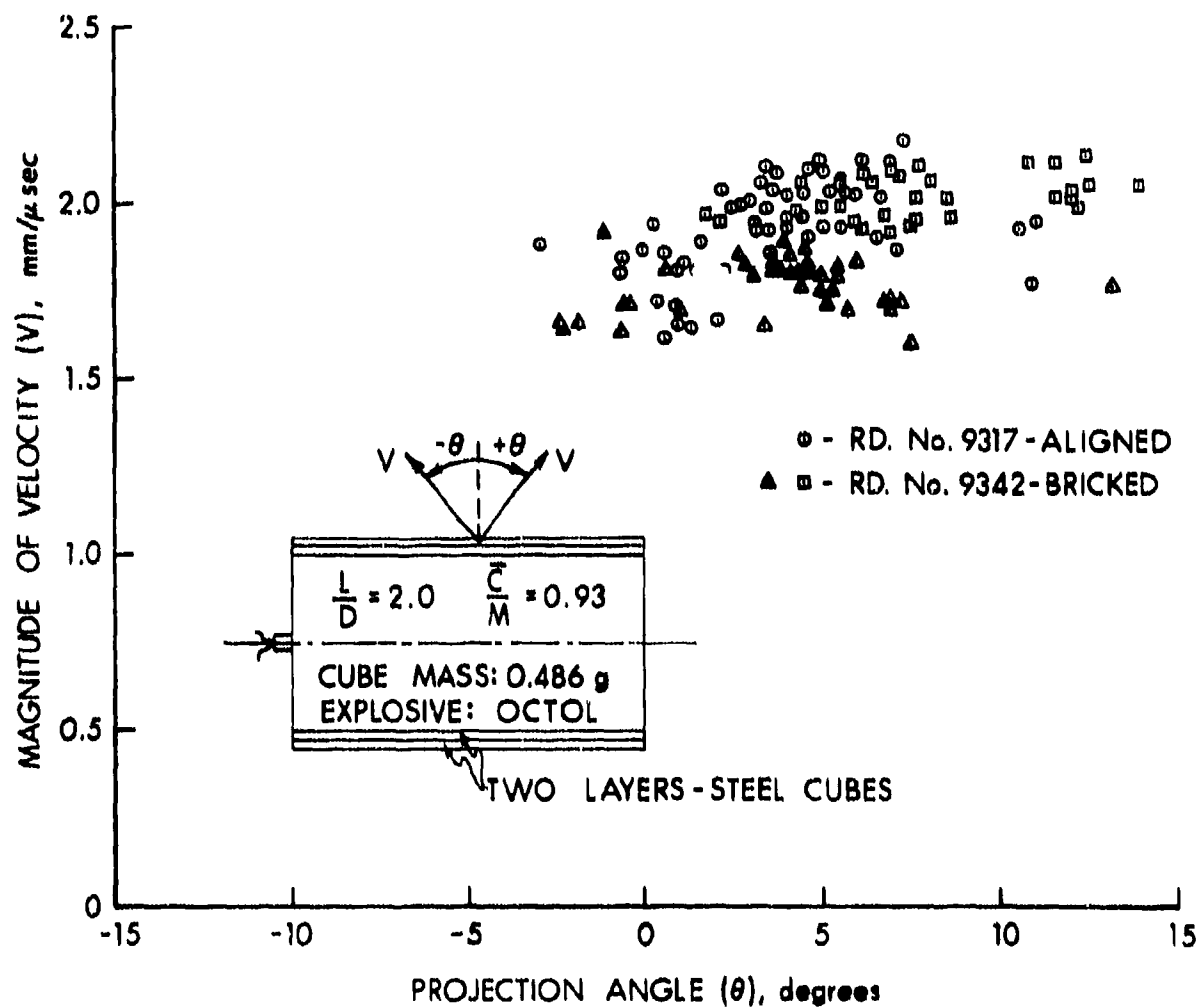


Figure 12. Double-Layered Discrete-Fragment Warheads:  
Fragment Speed Versus Projection Angle

In Figure 12 it is quite evident that there exists a significant variation of the magnitude of the velocity at any projection angle; this observation applies both to the aligned and bricked warheads. By comparison, if the data from the single fragment layer case of Figure 16 were plotted versus projection angle, as in Figure 12, only one fragment would appear at any particular projection angle. It is important to note, for reasons previously discussed, it was very difficult to identify the same fragment in two time-sequential, radiographic views for many of the fragments in the double-layered cases. Consequently, the only fragments that are plotted are those in which this identification was confidently made. Therefore, although the single fragment layer case cannot be compared with the double-layered case over the entire projection angle distribution, meaningful comparisons can be made over the projection angle range for which data were obtained. In the two examples depicted in Figure 12, the spread in the speeds ranges from 0.15 to 0.40 mm/ $\mu$ sec over the projection angle distribution. The most probable contributing cause of this spread in speed at a given projection angle is slippage between the layer fragments. Thus, instead of fragments leaving the warhead at a given angle having one particular velocity, collective effects result in a number of fragments with varying velocities at the specified angle.

It is lastly noted that the plotted speeds in Figure 12 have not been corrected for drag, which from the data was estimated to be causing a 4%-7% decrease in fragment speeds. This decrease was obtained by comparing single and double flash calculations of identical cubes. This calculation was also completed in the single layered cases; however, in these cases the drag was always negligible. Because of the lower cube masses (0.486 gm) in the double-layered warheads, drag is no longer negligible.

Shown in Figure 13 are the experimental results for single-layered fragments on an aluminum liner with aluminum endplates,  $L/D = 2.0$  cylindrical warhead. As shown, initiation was on the axis on the left side of the warhead. All the necessary data are given in Table I. This is the only test case reported with a liner and endplates. These results will be discussed in some detail in Section IV along with a similar test case without a liner and endplates.

### III. COMPUTATIONAL MODELING

The computer code that is being used for the computation modeling is a modified version of the HEMP<sup>4</sup> computer code. The HEMP code, which was originally developed at the Lawrence Livermore Laboratories, California, is a time-dependent, two-dimensional, Lagrangian finite-difference code.

---

<sup>4</sup>Wilkins, M. L., "Calculations of Elastic-Plastic Flow," *Methods of Computational Physics*, Vol. 3, edited by Alder, B., Fernback, S. and Rotenburg, M., Academic Press, NY, 1964.

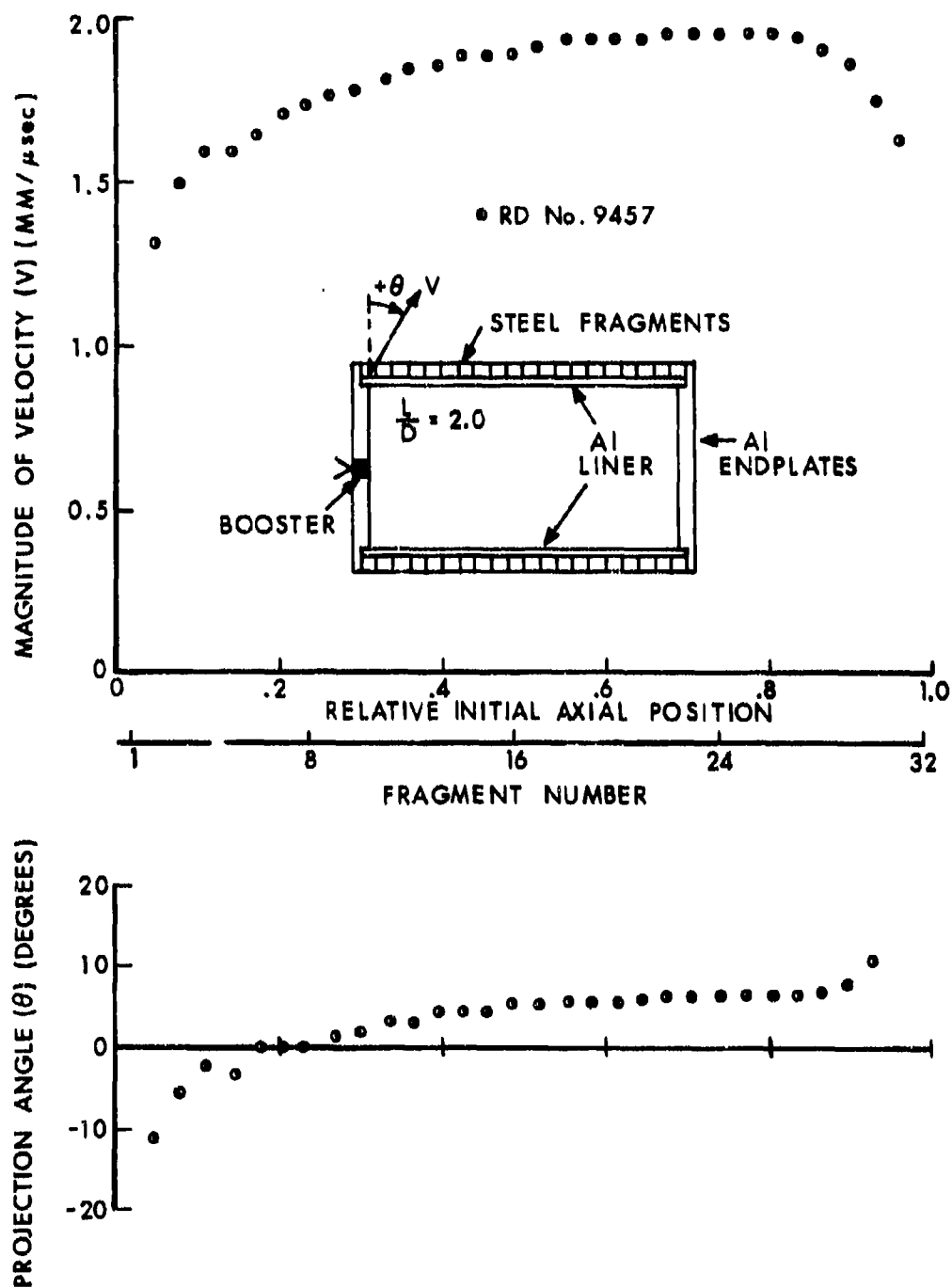


Figure 13. Preformed-Fragment Warhead with Al Liner and Al Endplates,  $L/D = 2.0$ : Fragment Speed and Projection Angle Distribution

If the standard form of the HEMP code is used to predict the performance of discrete-fragment warheads without including the effects of fragment separation and subsequent explosive gas leakage between fragments, the dashed line results shown in Figure 14 are obtained. Shown in Figure 14 is a comparison between these HEMP calculations and experimental data of fragment speed and projection angle distributions for an  $L/D = 1.0$  cylindrical warhead. In the HEMP calculations the fragments are modeled as a fluid, i.e., the fragments cannot accommodate a tensile force but they can be recompressed. This would be a logical approach with a continuum code since the fragments are not a continuum but discrete particles which will separate with the application of a small tensile force. It is obvious that this modeling is superior in predictive ability than the prediction of velocity and angle by Gurney and Taylor, also shown in Figure 14. However, the agreement between the HEMP computations and experiment is not as good as desired. Because of this and other objections<sup>5</sup>, modeling of the effects of fragment separation and explosive gas leakage between fragments was initiated to improve the overall predictive capability of the computations.

The discrete-fragment warhead (missile warhead) model presented involves the following three essential features: A) modeling of the discrete-fragments, B) modeling of fragment separation and subsequent explosive gas leakage and, C) criteria for fragment separation and method to determine this criteria.

#### A. Modeling of Discrete-Fragments

When discrete-fragments are placed on a cylindrical body, whether it be the bare explosive or a liner containing the explosive, (assuming conventional fragment shapes) air gaps will occur between the fragments in the circumferential direction. Consequently, the discrete-fragment casing forms a composite of metal and air. In reality, this is a three-dimensional system. However, the approach that was adopted with the two-dimensional modeling is similar to the methods used in the modeling of composite materials. The discrete metal-air composite casing (metal preformed-fragments) is modeled as a homogeneous continuous material of the same metal material as the experimental fragments, but with the requirement that the total mass of the new continuous metal casing equal the total mass of all the fragments on the experimental warhead. For example, in the case of cubical fragments, the resulting continuous metal casing wall thickness in the model will be less than one of the sides of

---

<sup>5</sup>Karpp, R. R. and Predebon, W. W., "Calculations of Fragment Velocities from Fragmentation Munitions," First International Symposium on Ballistics, Orlando, Florida, 13-15 November 1974, Section IV, pp. 145-176, Proceedings Published by American Defense Preparedness Association, Union Trust Building, Washington, DC.

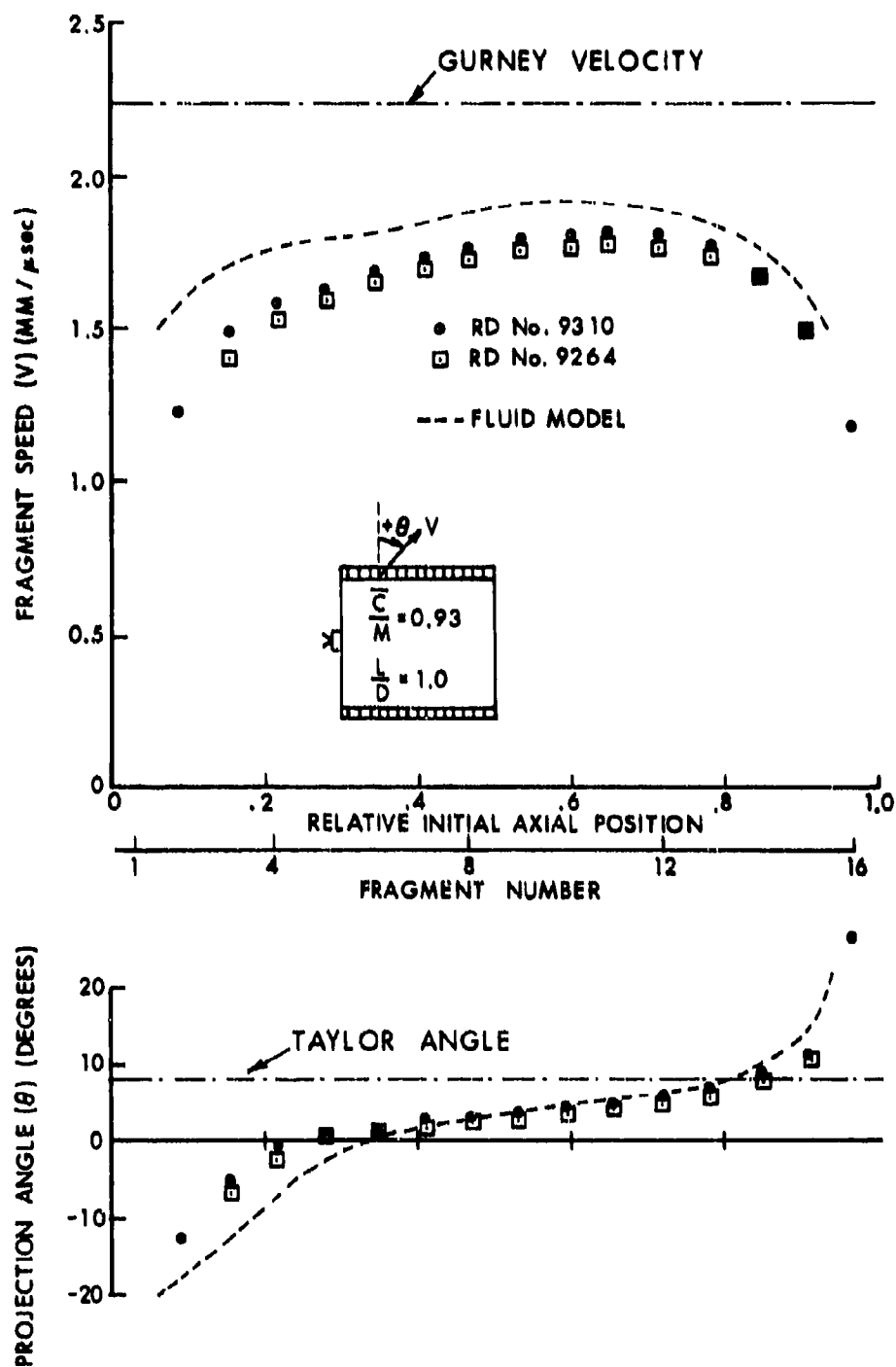


Figure 14. Comparison of Gurney Velocity and Taylor Angle with HEMP (Fluid Model) Computations and Experimental Data,  $L/D = 1.0$  Cylindrical Preformed-Fragment Warhead

an actual cubical fragment. For a cylindrical warhead, the modeled casing outside diameter for a given explosive diameter is obtained from

$$M_T = \sum_i m_i = \rho_f \left\{ \frac{\pi}{4} l_w (D_M^2 - D_{III}^2) \right\},$$

where  $M_T$  is the measured total fragment mass (plus liner mass if the warhead has a liner),  $m_i$  are the measured individual fragment masses,  $\rho_f$  is the fragment density,  $l_w$  is the total length of the fragments on the warhead,  $D_{III}$  is the measured diameter of the explosive and  $D_M$  is the outside diameter of the continuous metal casing to be computed. If one ignores the air gap between the fragments and uses the fragment cube dimension as the continuous casing wall thickness, then for the cases reported in Sections II and IV, the modeled total mass will be as much as 6% greater than the actual total mass.

#### B. Fragment Separation and Explosive Gas Leakage

The general ideas of the model for fragment separation and explosive gas leakage will be presented here; however, the specific details and equations have been presented in an earlier report<sup>5</sup>.

The HEMP code models continuum behavior in general. However, in reality, when fragment separation occurs a continuous casing circumference ceases to increase. But the standard form of the code causes the casing to remain continuous. This treatment tends to yield a higher radial acceleration and thus a higher final fragment velocity. This can be corrected by computing the true force acting on an element of the casing. The true force is computed in the code by reducing the pressure acting on the interface of the casing by the factor  $R_b/R$ , where  $R_b$  is the radius at fragment separation and  $R$  is the current radius. At present,  $R_b$  must be determined by experiment. After fragment separation, i.e.,  $R > R_b$ , a void appears between fragments and gas leakage occurs.

This effect is modeled in the code by calculating the rate of efflux from an ideal nozzle passing its maximum rate of flow. The rate of efflux is computed in the code for every cycle, and the mass leaked for a single cycle is the product of the mass rate and the cycle time increment. In this manner, the model accounts for gas leakage between fragments after casing breakup. Gas leakage reduces the pressure accordingly. Lastly, to simulate a loss in circumferential stress upon casing breakup, the yield strength of the fragment material is set equal to zero when  $R > R_b$ .

#### C. Criterion for Fragment Separation

Currently, the criterion for fragment separation,  $R_b$ , is an empirically determined quantity. As discussed in Section II the fragments

are all premarked and recovered in a soft recovery medium (Celotex) after firing. The recovered fragments are weighed and measured for their dimensions. Obtained from these measurements is the fragment plastic deformation due to the explosive loading (or final dimensions). Since its original dimensions are known a straight forward calculation determines the corresponding radius of the warhead at which the fragments separated. (The elastic displacements are neglected in this analysis). For the case of cubical fragments on bare explosive for  $L/D = 1.0$  and  $2.0$  cases, the expansion ratio at fragment separation, i.e.,  $R_p/R_o$  where  $R_o$  is the inside radius of the casing, was found to be 1.2. The recovered fragment measurements and expansion ratios are tabulated in Table I. This criterion for fragment separation is empirical; the criterion will not be applicable in general. Thus, the next refinement in this analysis is to relate this criterion to a fundamental material property.

#### IV. COMPARISON BETWEEN COMPUTATIONAL AND EXPERIMENTAL RESULTS

In Figures 15-17 are shown comparisons between the calculations with the discrete-fragment model (labeled Elastic-Plastic with Gas Leakage Model) and experimental results. In Figure 15 and 16 the calculated fragment speed and projection angle distributions are compared with the experimental data for  $L/D = 1.0$  and  $2.0$  cylindrical warheads, respectively. Data from two test firings are plotted in each figure. In both cases the agreement between computation and experiment is extremely good. Also shown in Figures 15 and 16 are the calculations without the discrete-fragment model, namely, a fluid model, and the Gurney velocity and Taylor angle predictions. Shown in Figure 17 is a comparison between the computations and experimental data for the same case as shown in Figure 16 except with dual-end axial initiation. Again the agreement between computation and experiment is very good. Note that the computations model the region where the two detonation waves collide (higher pressure region) at 0.5 relative initial axial position.

Returning to the test results shown in Figure 13, note that the warhead configuration in Figure 13 is similar to the configuration in Figure 16. Both are  $L/D = 2.0$  cylindrical warheads with the same explosive material, fragment material and size, and with essentially the same explosive diameter. However, the test warhead in Figure 13 has a liner between the explosive and fragments, and endplates. The reasons given for placing the liner between the fragments and the explosive are often varied. It was the intent of this initial experiment, in conjunction with computational modeling (yet to be performed), to help explain the effect of a liner on warhead performance. Due to the additional width of the Al liner, the inside fragment radius increased, which resulted in more fragments on the warhead, and thus a larger total metal weight, and lower C/M. These data are given in Table 1 by Rd. No. 9457. Consequently, the results of Figures 13 and 16 cannot be directly compared. However, it is the authors' judgment at this time, based on these data and other

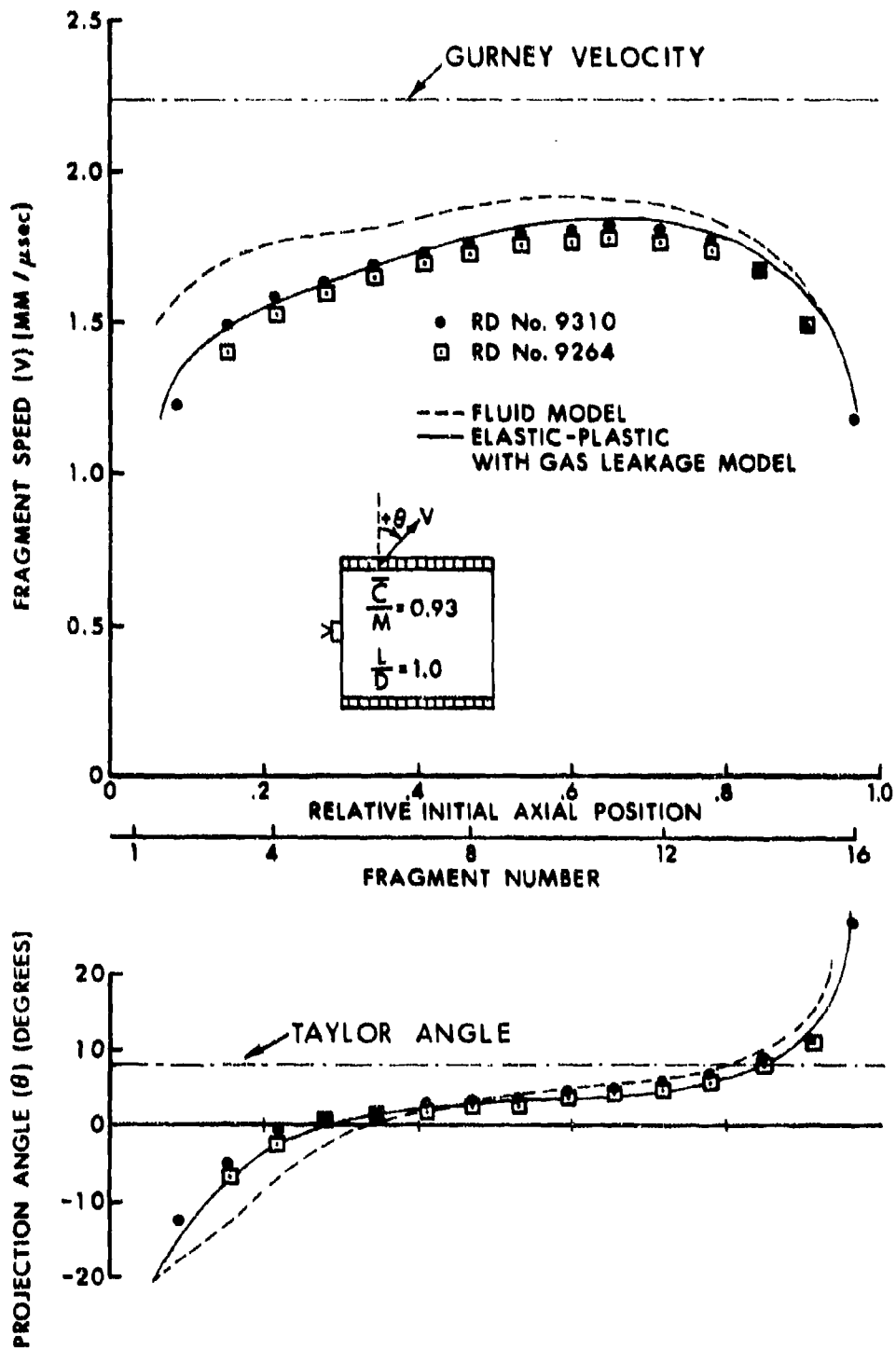


Figure 15. Comparison of Fluid Model Computations and Discrete-Fragment Model Computations with Experimental Data,  $L/D = 1.0$  Cylindrical Preformed-Fragment Warhead

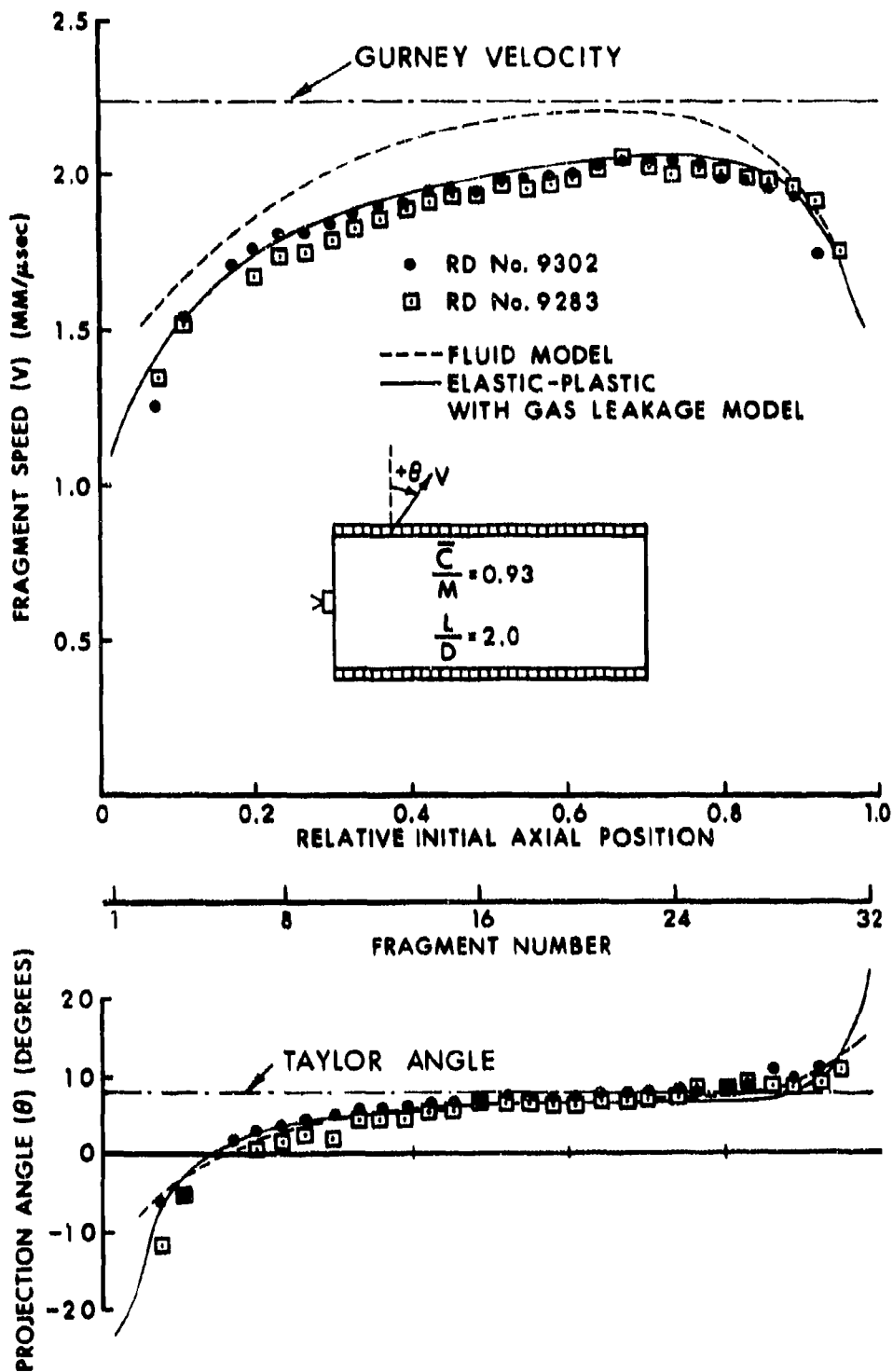


Figure 16. Comparison of Fluid Model Computations and Discrete-Fragment Model Computations with Experimental Data,  $L/D = 2.0$  Cylindrical Preformed-Fragment Warhead

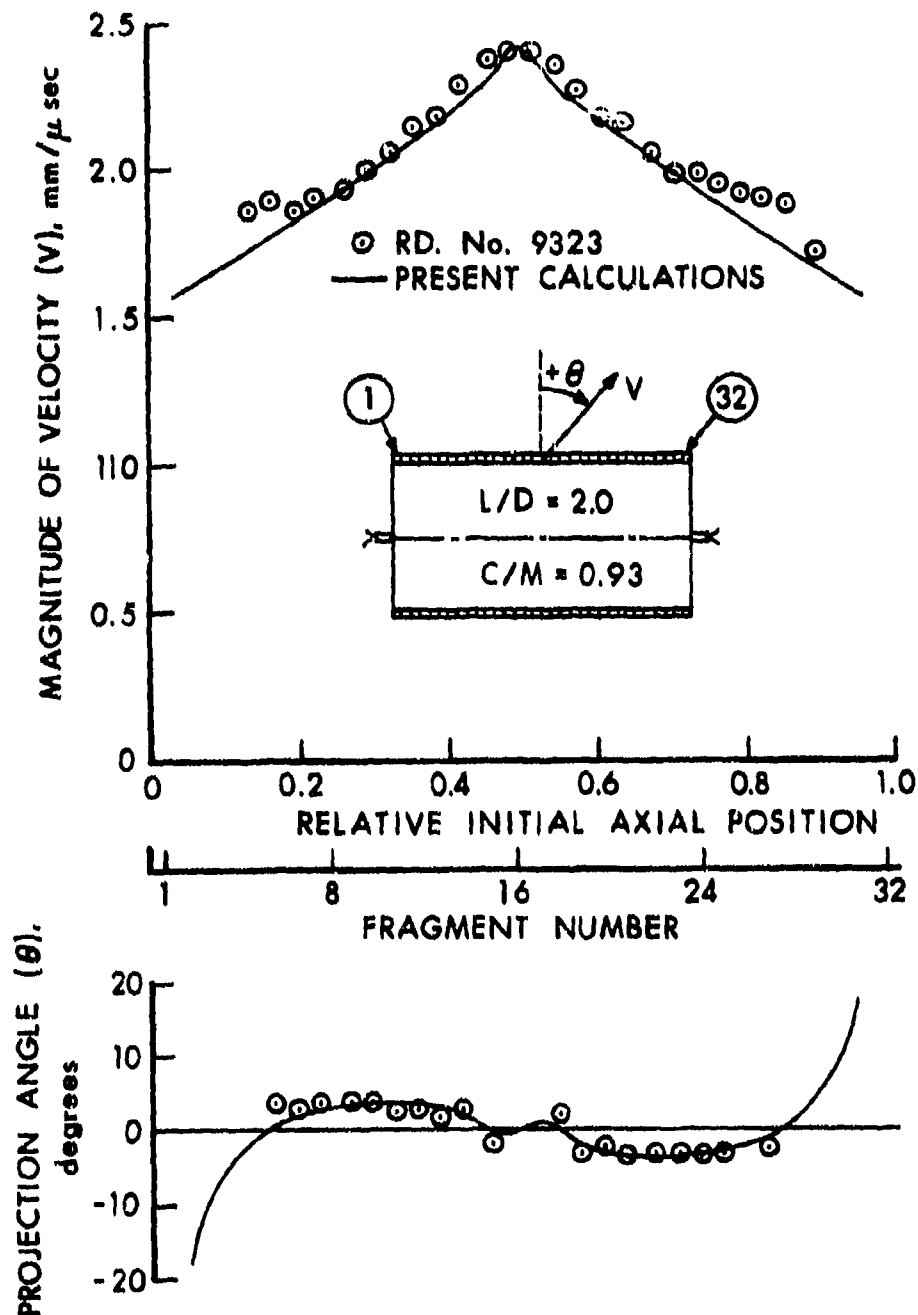


Figure 17. Comparison of Discrete-Fragment Model Computations with Experimental Data for  $L/D = 2.0$  Cylindrical Preformed-Fragment Warhead with Dual End Axial Initiation

calculations, that the effect of a liner is to contain the explosive gases for a longer period of time. This in turn causes leakage of explosive gases between fragments to occur at a larger expansion ratio, resulting in a higher final fragment speed, as compared to the case without a liner (assuming all other quantities being equal). This can be illustrated from a plot<sup>6</sup> of calculated fragment speed versus time (from detonation) for these cases. From a plot of this type one observes that fragment separation and leakage occurs during the initial, approximately exponential, acceleration rise. By placing a liner between the fragments and explosive, one can prolong fragment separation and subsequent leakage until the fragment speed versus time profile flattens, which then results in a higher final fragment velocity. From these and other computations, it is estimated that up to approximately a 10% increase in final fragment velocity can be obtained with a liner between the fragments and explosive versus the case without a liner.

Having demonstrated extremely good agreement between the present calculations and experimental data for both  $L/D = 1.0$  and  $2.0$  cylindrical warheads with single-end and dual-end axial initiation, the computations were then confidently utilized, without experimental verification, to study the effect of initiation posture on warhead performance. Shown in Figure 18 are the nine initiation postures that were computed. The cylindrical warheads that are drawn in Figure 18 are all with a length ( $L$ ) to diameter ( $D$ ) ratio of two and initiated as shown. The first case of dual end axial booster initiation, i.e., initiation with two 19.05 mm diameter explosive boosters, is shown in Figure 17. The computational results of the remaining eight cases are shown respectively in Figures 19-26. Shown in Figure 17 and Figures 19-26 is the effect of a large variety of initiation postures on warhead performance. The general idea of this set of computations is, on the one hand, to demonstrate the versatility and generality of this computational tool, and on the other hand to aid in the understanding of the effect of initiation posture on warhead performance. Furthermore, should the initiation posture of interest lie somewhere between these cases, a simple interpolation of the already computed cases is all that is required for a first approximation of the warhead performance. Similarly, since the computational results are general, i.e., scalable, then if the geometry of interest is not precisely the same as the cases calculated, these results can be scaled up or down assuming proper scaling procedures are followed. Lastly, it is worth while to note that axial line initiation, Figure 26, is the one case of the initiation variations studied in which the fragment projection angle and speed distribution are significantly different from the dual end axial initiation case, Figure 17.

Shown in Figures 27 through 30 are the computational results for two different internal cavity sizes and materials for the same general  $L/D = 2.0$  cylindrical geometry. Shown in Figure 27 are the results for

<sup>6</sup>Karpp, R. R. and Predebon, W. W., "Calculations of Fragment Velocities from Fragmentation Munitions," p. IV-164.

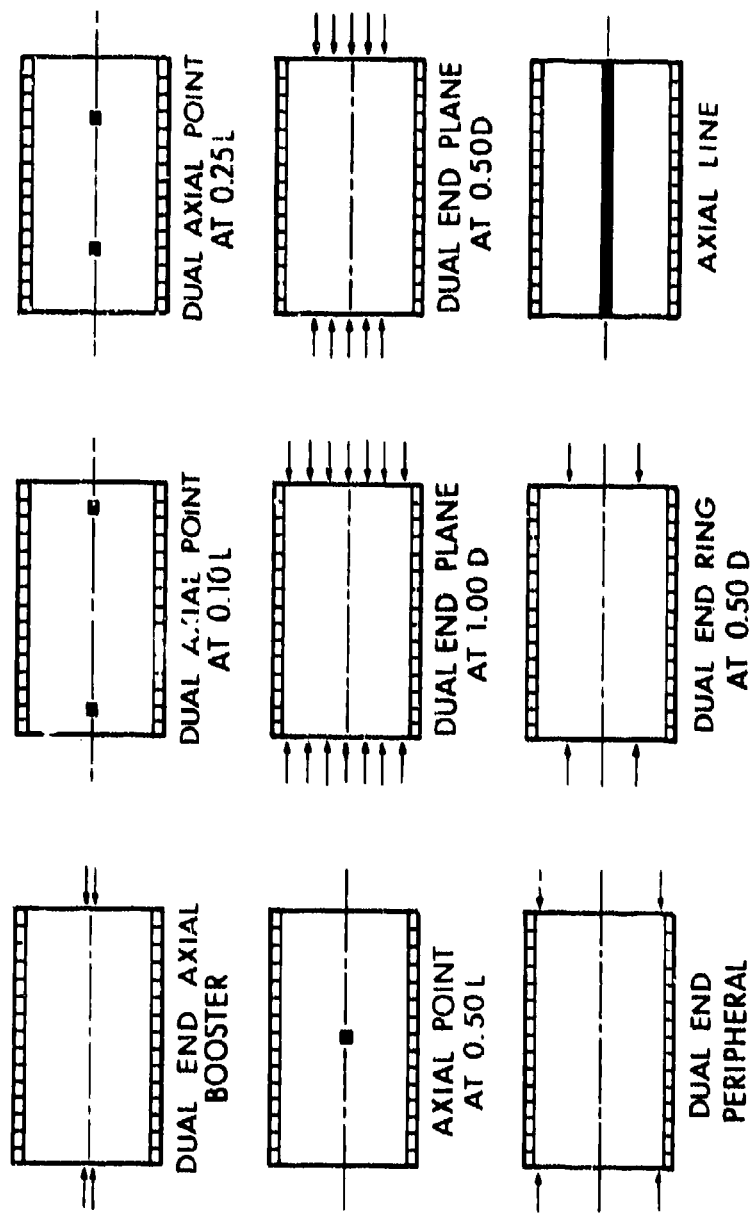


Figure 18. Initiation Postures

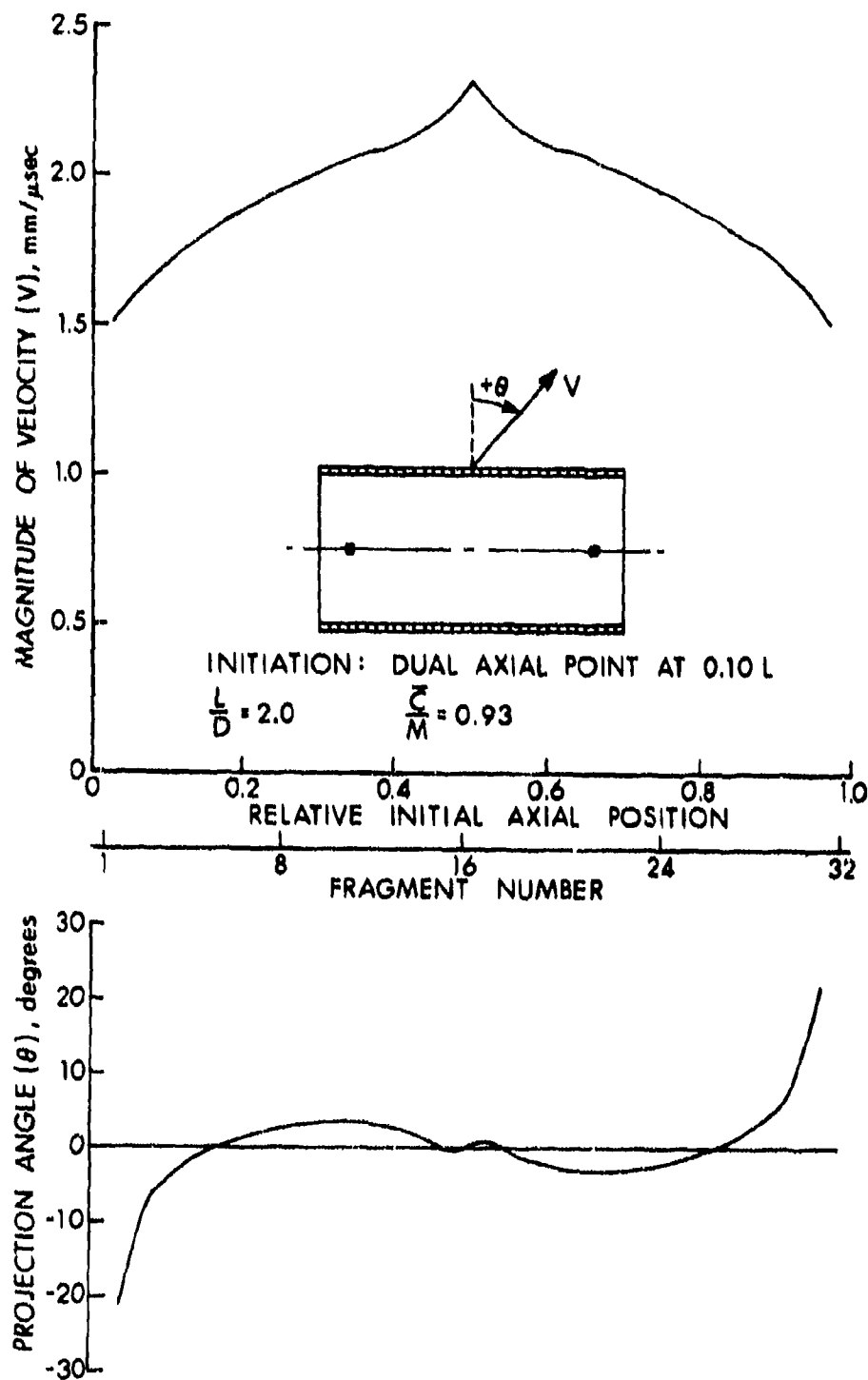


Figure 19. Calculations of Fragment Speed and Projection Angle Distributions for  $L/D = 2.0$  Cylindrical Preformed-Fragment Warheads with Dual Axial Point Initiation at 0.10 L.

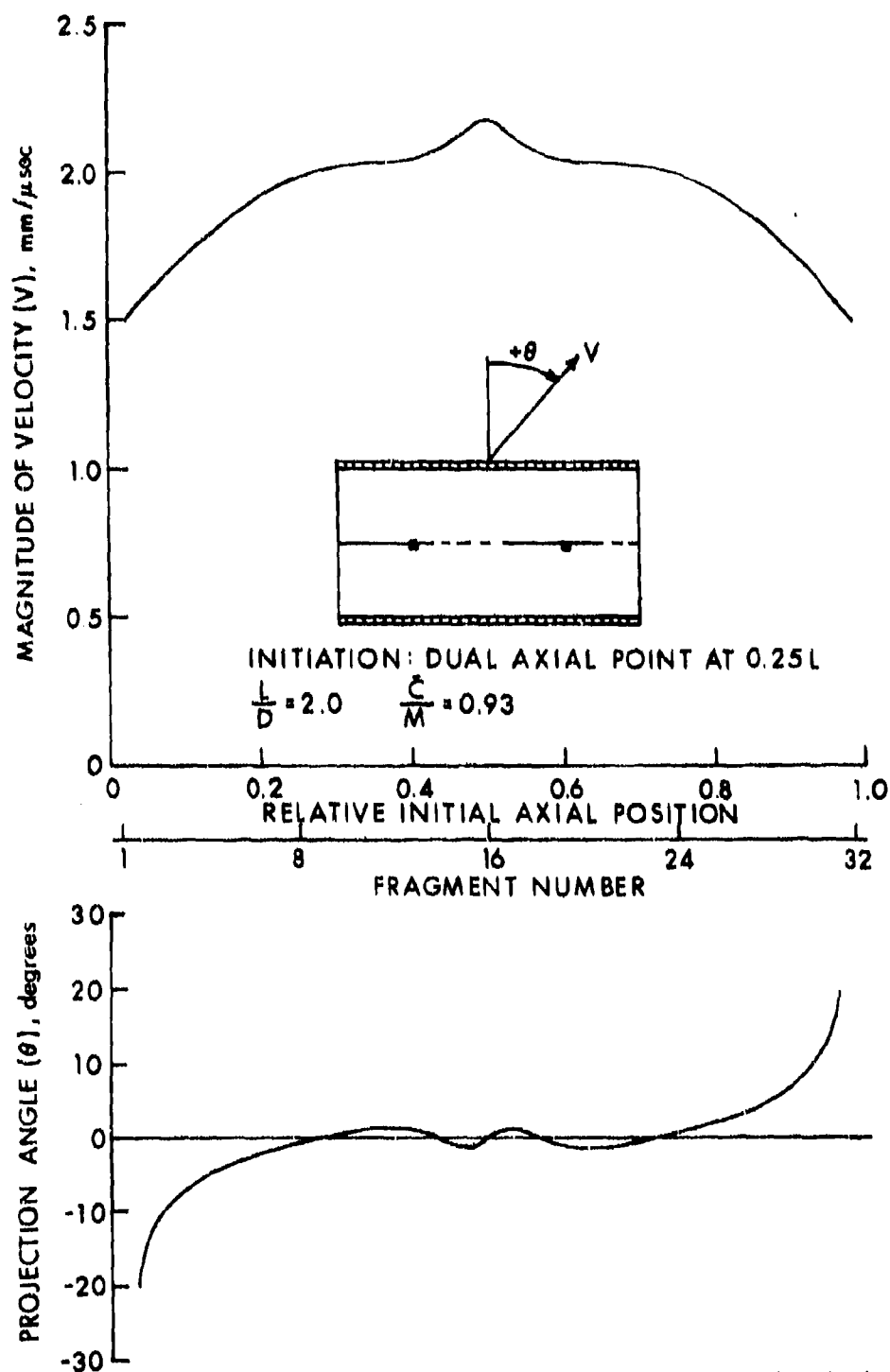


Figure 20. Calculations of Fragment Speed and Projection Angle Distributions for  $L/D = 2.0$  Cylindrical Proformed-Fragment Warheads with Dual Axial Point Initiation at 0.25 L.

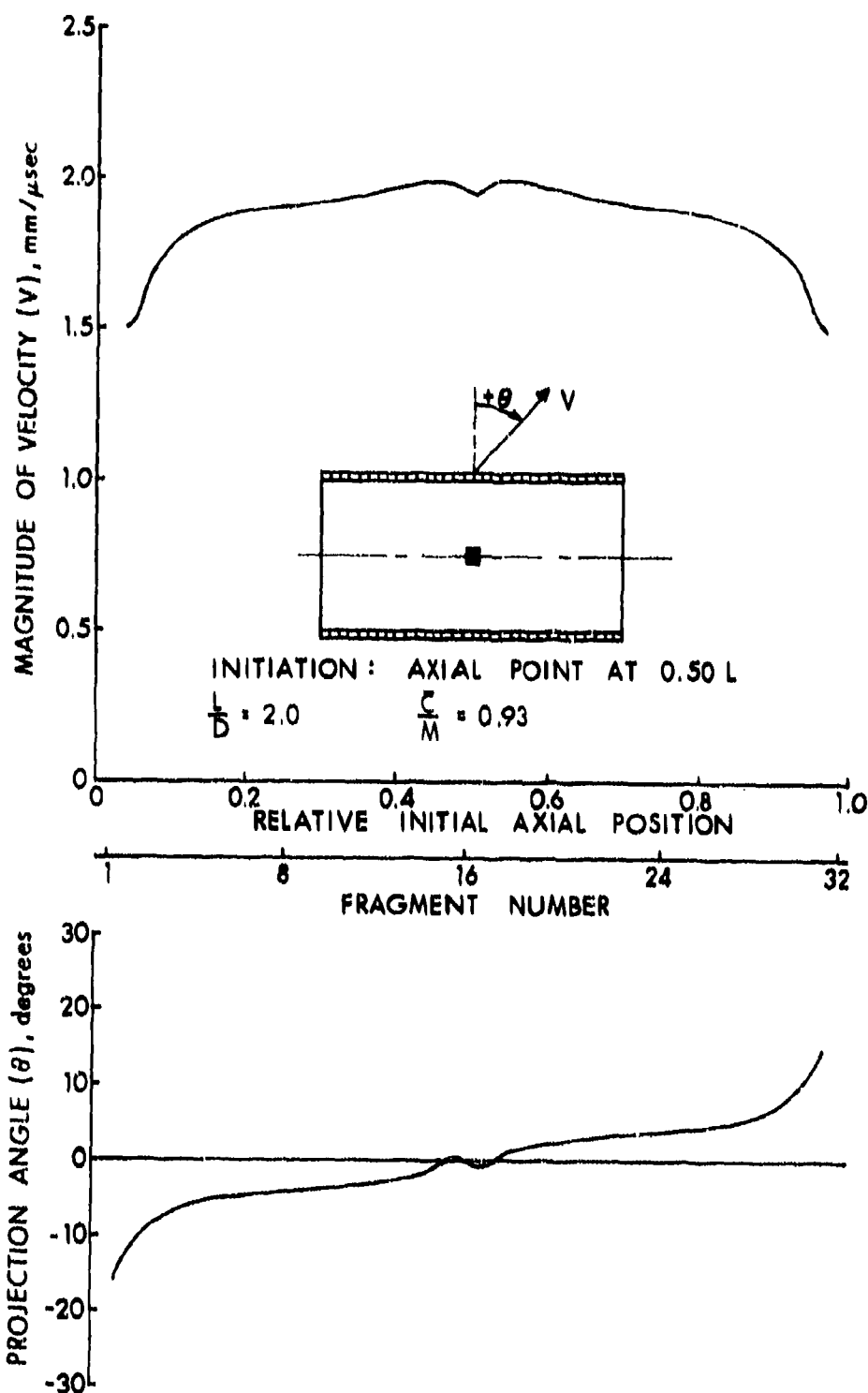


Figure 21. Calculations of Fragment Speed and Projection Angle Distributions for  $L/D = 2.0$  Cylindrical Preformed-Fragment Warheads with Axial Point Initiation at 0.50 L.

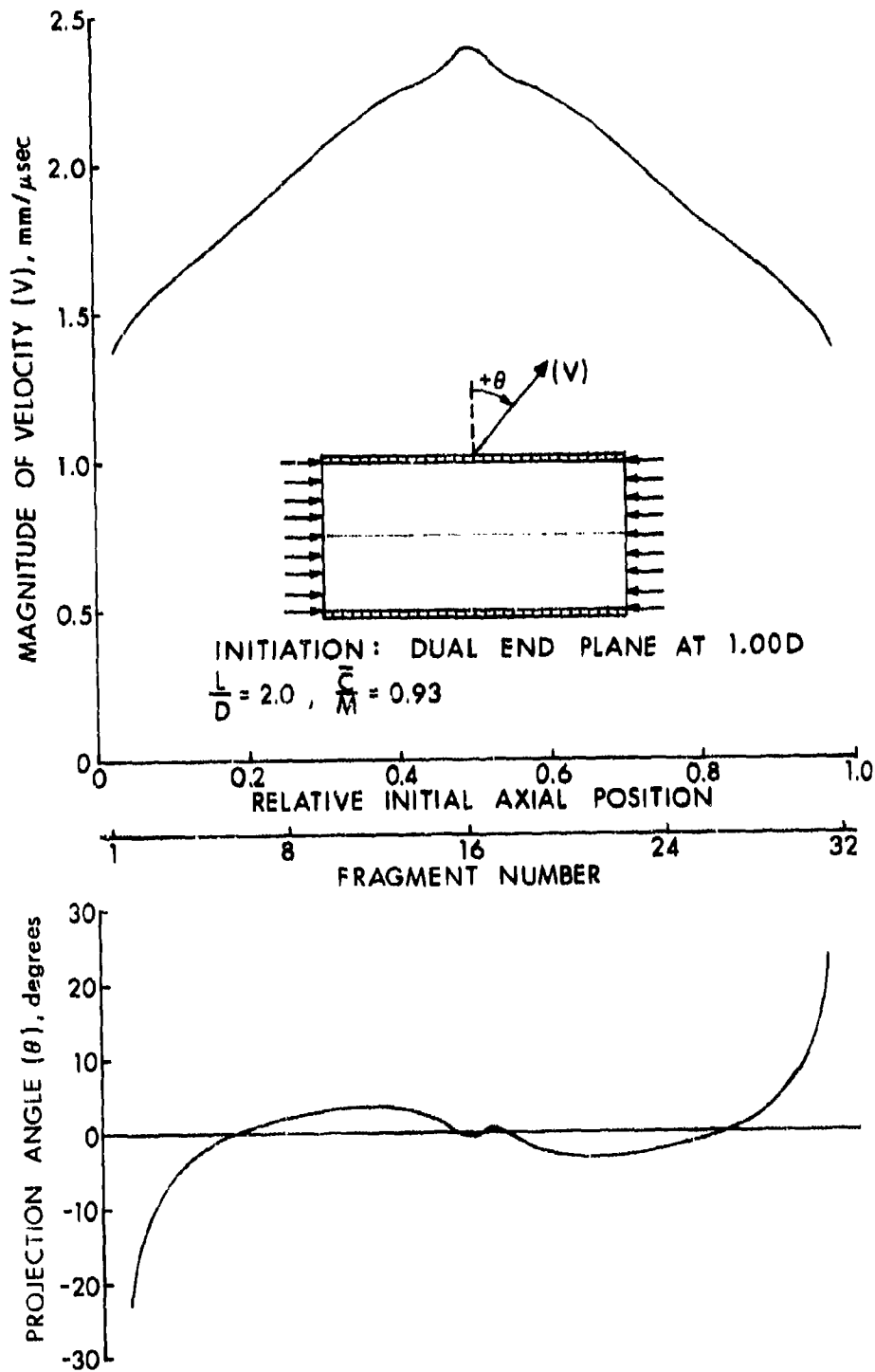


Figure 22. Calculations of Fragment Speed and Projection Angle Distributions for  $L/D = 2.0$  Cylindrical Preformed-Fragment Warheads with Dual End Plane Initiation at 1.00 D

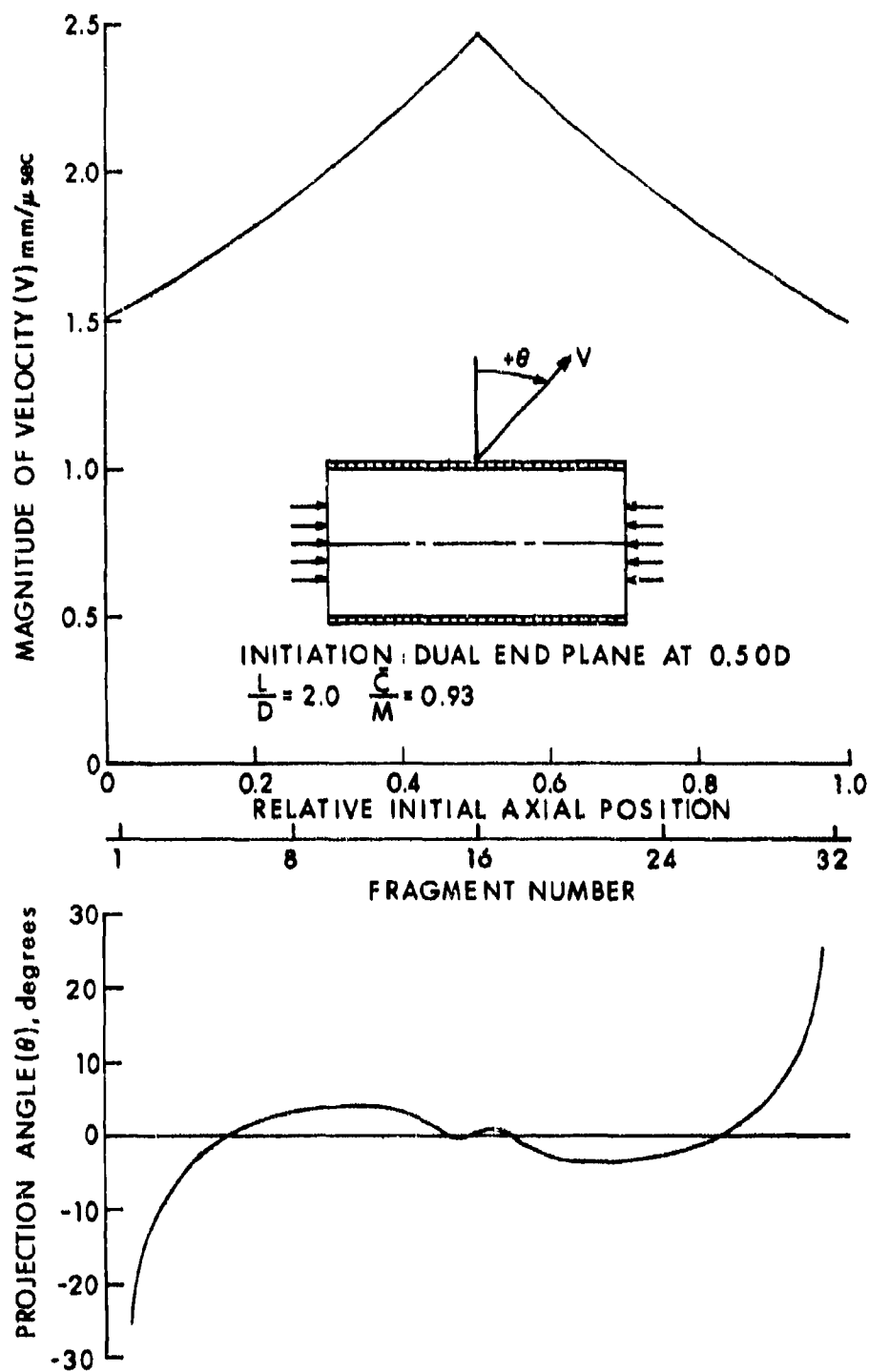


Figure 23. Calculations of Fragment Speed and Projection Angle Distributions for  $L/D = 2.0$  Cylindrical Preformed-Fragment Warheads with Dual End Plane Initiation at 0.50 D

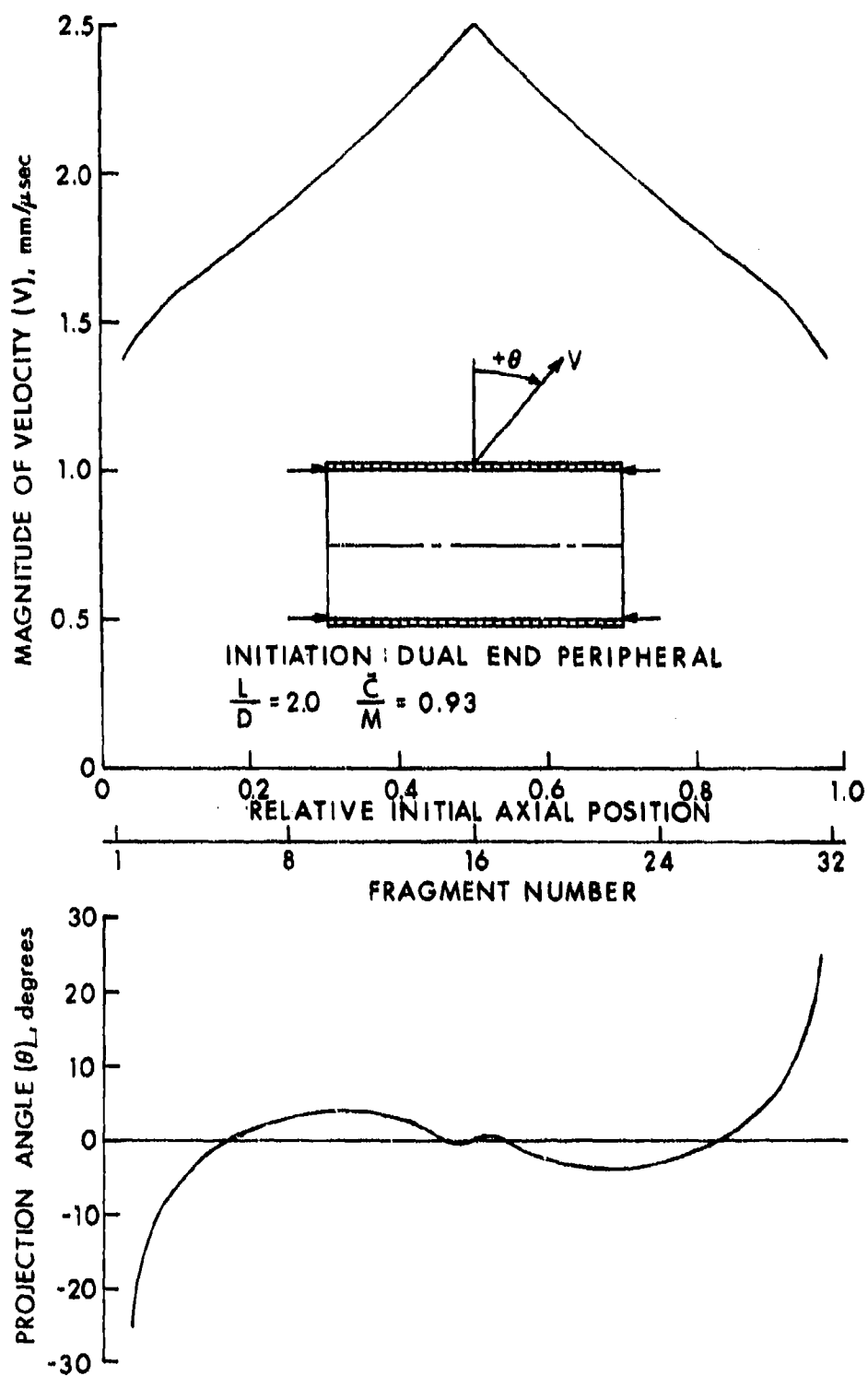


Figure 24. Calculations of Fragment Speed and Projection Angle Distributions for  $L/D = 2.0$  Cylindrical Preformed-Fragment Warheads with Dual End Peripheral Initiation

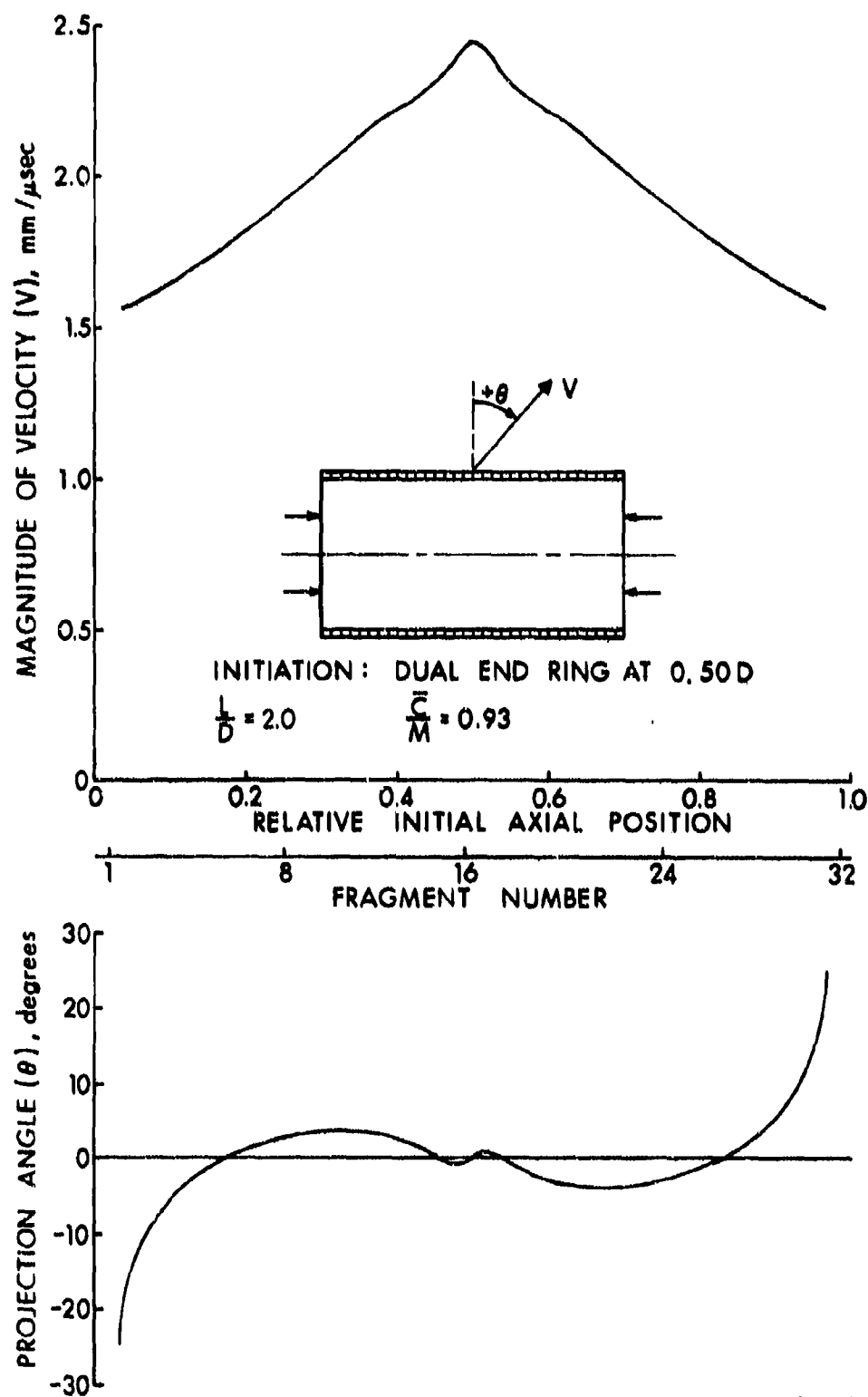


Figure 25. Calculations of Fragment Speed and Projection Angle Distributions for  $L/D = 2.0$  Cylindrical Preformed-Fragment Warheads with Dual End Ring Initiation at 0.50 D

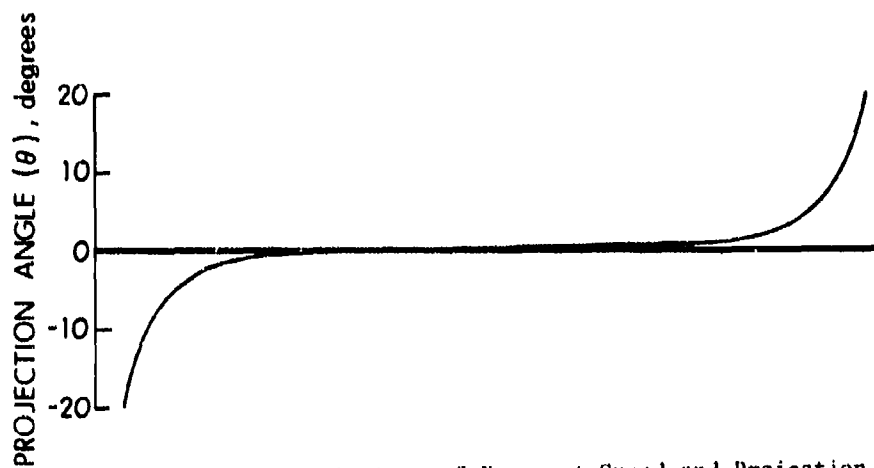
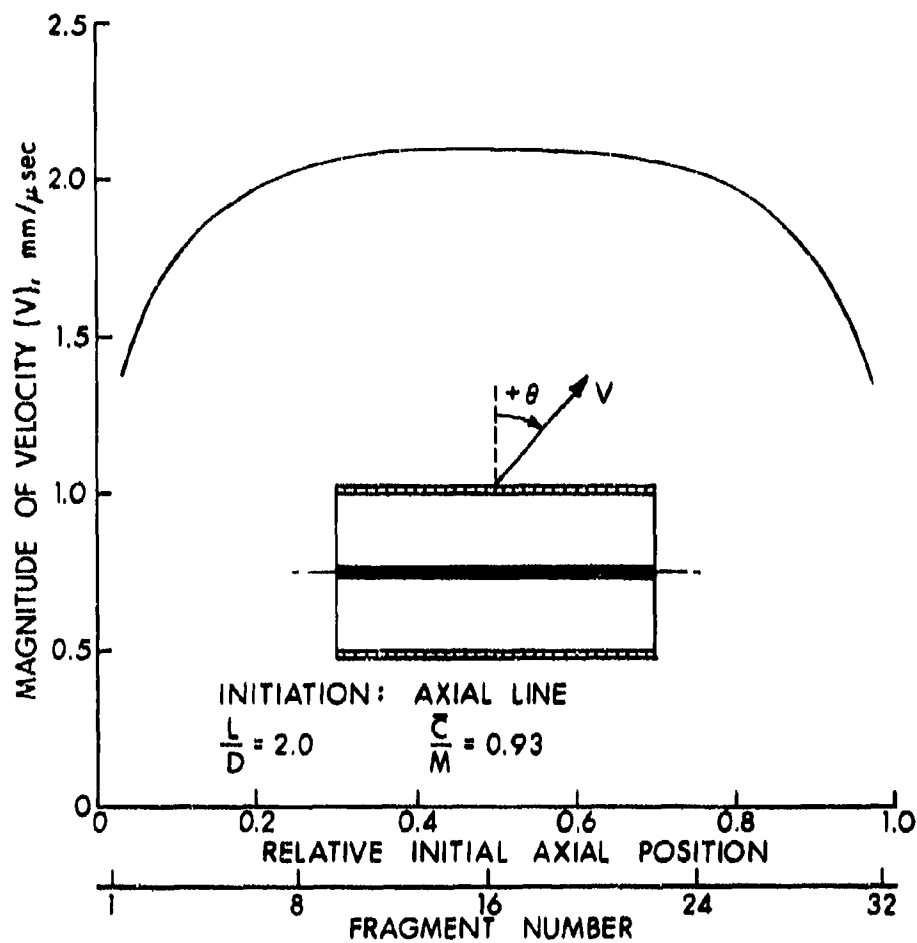


Figure 26. Calculations of Fragment Speed and Projection Angle Distributions for  $L/D = 2.0$  Cylindrical Preformed-Fragment Warheads with Axial Line Initiation

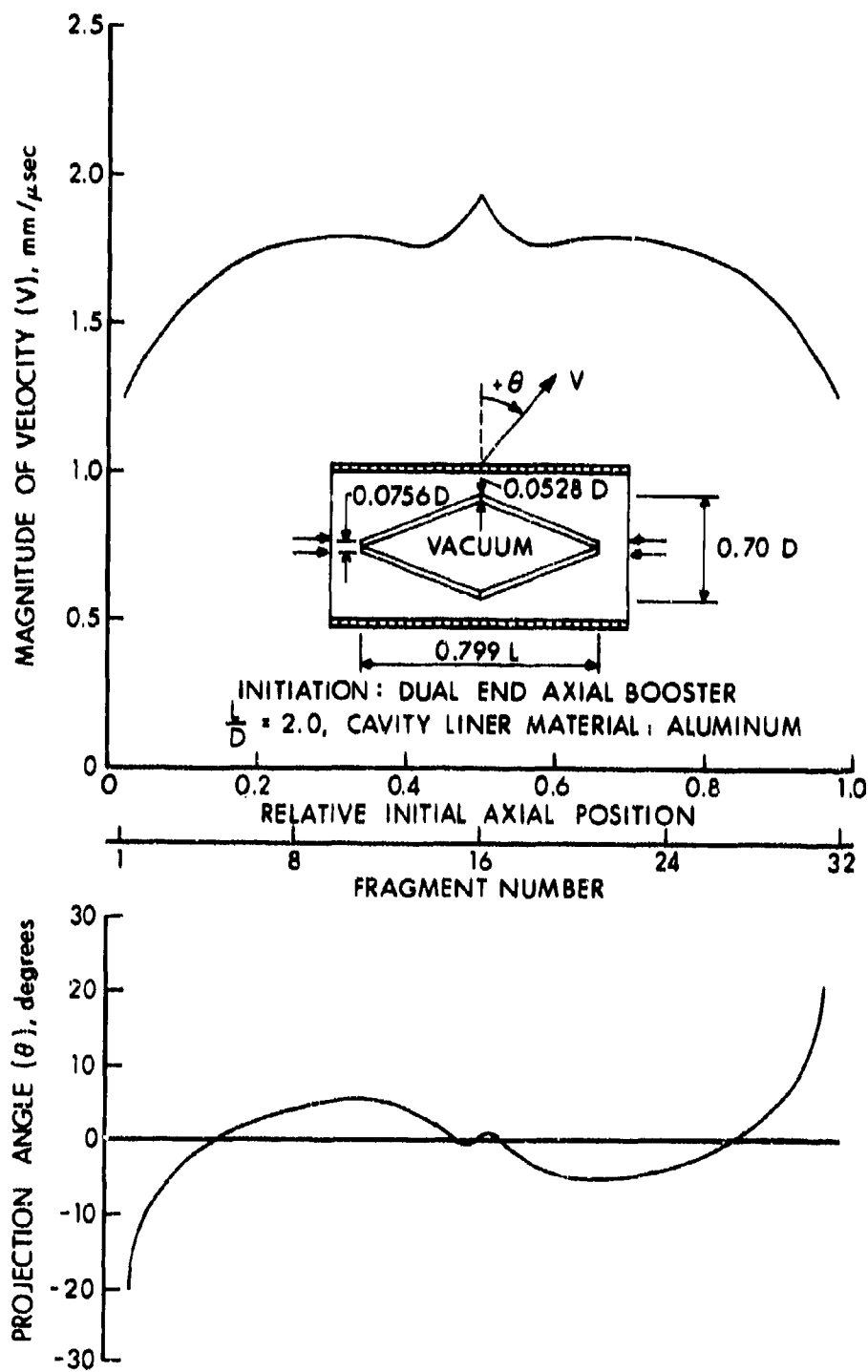


Figure 27. Calculations of Fragment Speed and Projection Angle Distributions for an  $L/D = 2.0$  Cylindrical Preformed-Fragment Warhead with Internal Aluminum Cavity Liner and Dual End Axial Initiation

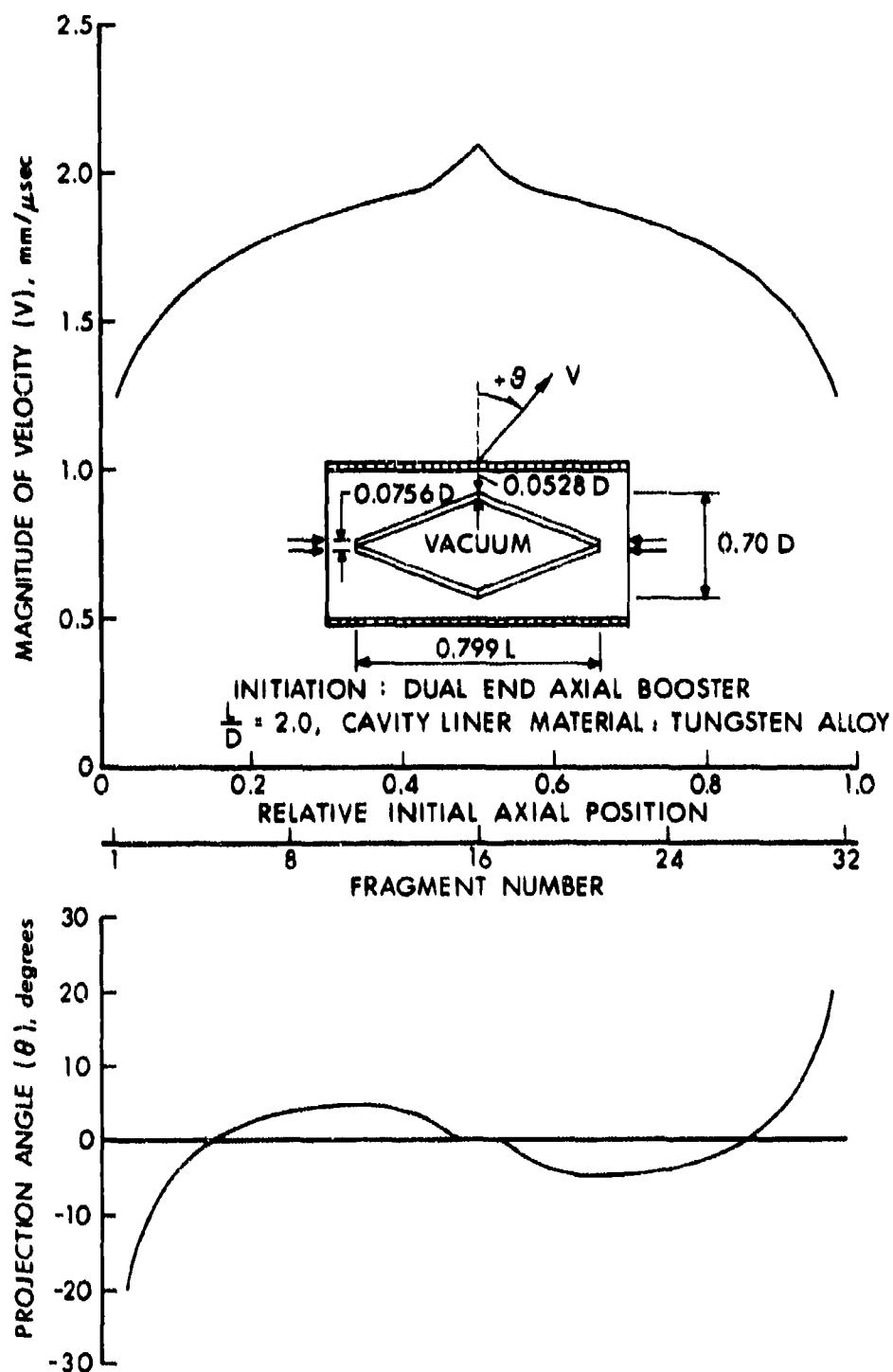


Figure 28. Calculations of Fragment Speed and Projection Angle Distributions for an  $L/D = 2.0$  Cylindrical Preformed-Fragment Warhead with Internal Tungsten Alloy Cavity Liner and Dual End Axial Initiation

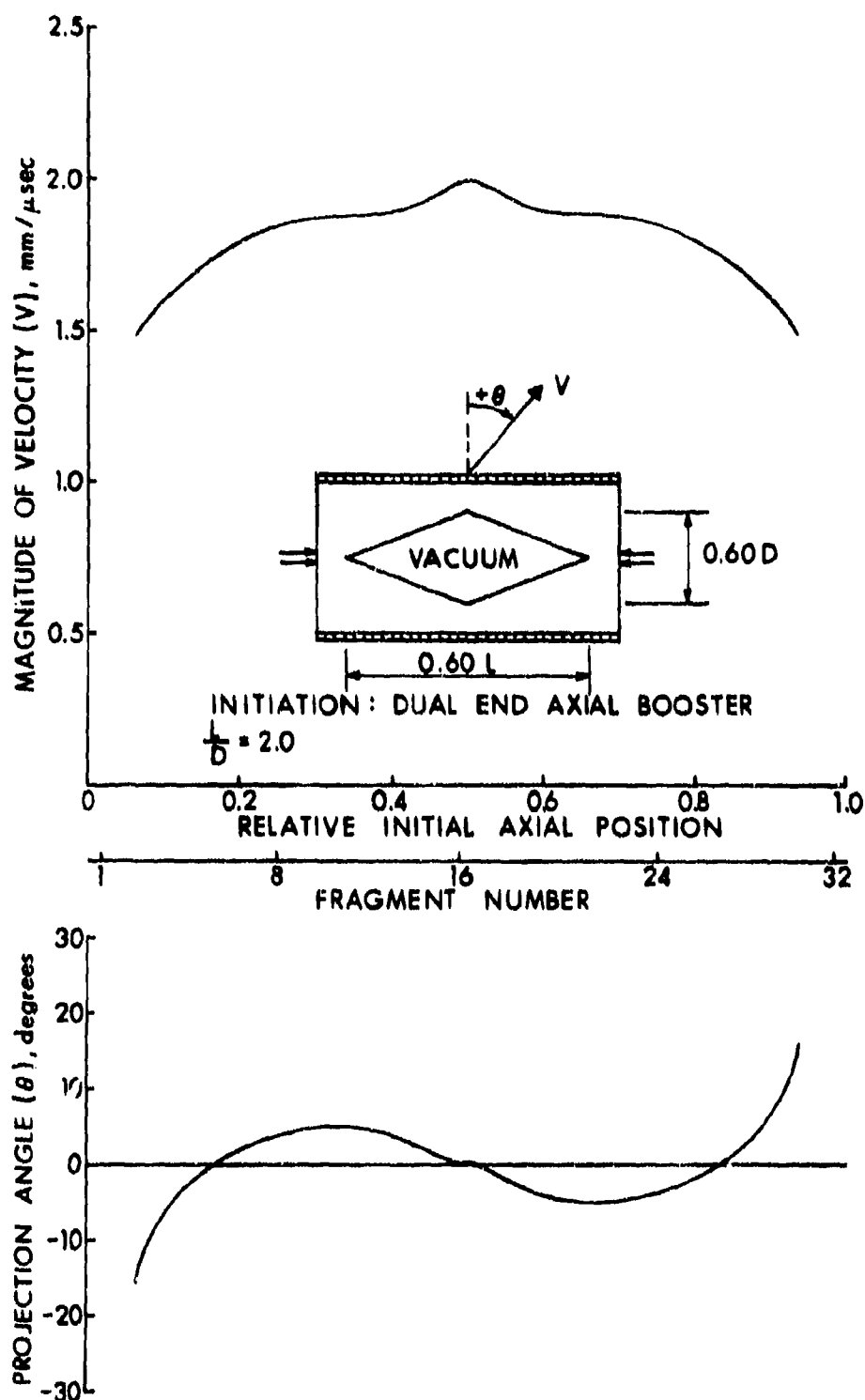


Figure 29. Calculations of Fragment Speed and Projection Angle Distributions for an  $L/D = 2.0$  Cylindrical Preformed-Fragment Warhead with an Internal Cavity Modeled as a Vacuum and Dual End Axial Initiation

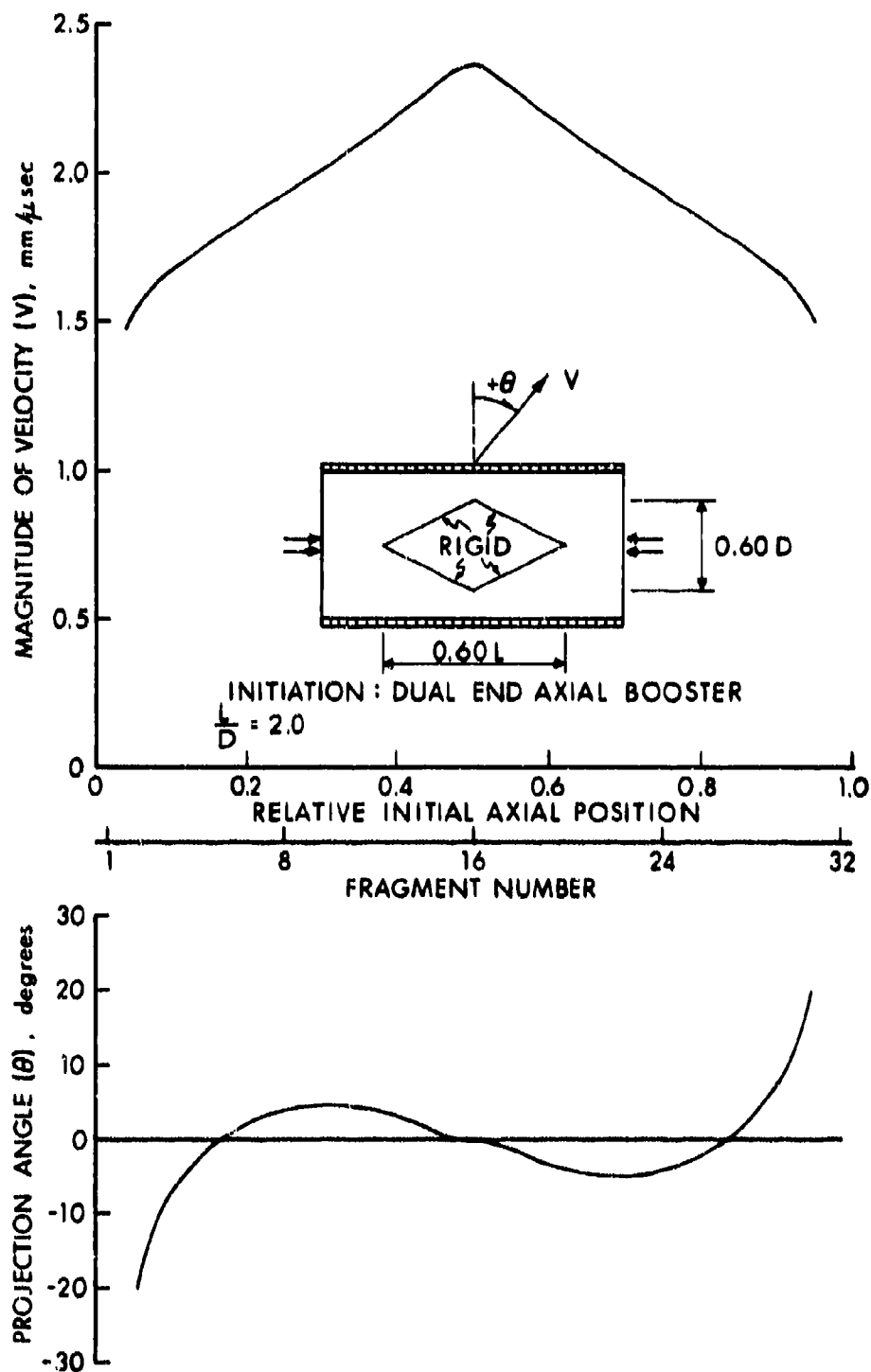


Figure 30. Calculations of Fragment Speed and Projection Angle Distributions for an  $L/D = 2.0$  Cylindrical Preformed-Fragment Warhead with an Internal Cavity Modeled as Rigid and Dual End Axial Initiation

the case with an aluminum cavity liner material with the dimensions as indicated. Comparing the results shown in Figure 27 with those in Figure 17 it can be seen that although the projection angle distribution is only slightly altered, the fragment speed is significantly reduced.

The computational results with a tungsten alloy ( $\rho = 16890 \text{ KG/M}^3$ ) cavity liner material for the same cylindrical geometry and cavity shape given in Figure 27 are shown in Figure 28. As expected, due to the higher density cavity liner material the fragment speed distribution is somewhat higher than with aluminum; however, the fragment projection angle distribution is not noticeably altered. It is important to note that these results are for one cavity shape and therefore are not necessarily true for all cavity shapes and sizes. In Figures 29 and 30 are shown the computational results for a slightly different cavity size where the cavity is modeled either as a vacuum (Figure 29) or as a cavity whose boundaries are rigid (Figure 30) for all time. The purpose of these two computations is to provide a qualitative lower (Figure 29) and upper (Figure 30) bound on fragment speed and projection angle distributions that can be expected for the cylindrical geometry and cavity shape shown.

## V. CONCLUSIONS AND RECOMMENDATIONS

A discrete-fragment warhead (missile warhead) computational modeling capability has been developed which is capable of modeling with a satisfactory degree of confidence the performance of a large variety of axisymmetric warhead configurations. The computational warhead model includes the ability to model the effects of varying L/D, fragment material and size, explosive material, initiation posture, and internal cavity material and shape. It is felt that the modeling capability can be extended to include two layers of fragments on the warhead, a liner between the fragments and the explosive, and end confinement. The experiments were completed for these cases and are discussed in Section II.

Future efforts should include additional experiments and computational modeling with different liner materials, shapes and sizes, and end confinement to understand fully the influence of these variables on warhead performance. Also, future work should include generalization of the empirical criterion for fragment separation to a more fundamental criterion. For example, material properties, such as the total plastic strain to failure, might be used to predict fragment separation.

It is also believed that the modeling capability can successfully be applied to certain aspects of eccentric warheads (a three dimensional problem). However, while some degree of success may be had, in order to model eccentric warheads properly, a three dimensional computer code is needed.

#### ACKNOWLEDGEMENTS

The authors wish to thank Dr. Robert R. Karpp for the many helpful technical discussions during the course of the work. Also the authors are grateful to Mr. G. Gentle and Mr. Carroll West for their assistance with the experimental program.

# LIST OF SYMBOLS

$\bar{C}/M$	Nominal charge (explosive) mass to metal mass (fragment + liner) ratio
$D_{HE}$	Explosive diameter
$D_M$	Calculated outside diameter of continuous metal casing model, from $M_T = \rho_f \{ \pi/4 L_W (D_M^2 - D_{HE}^2) \}$
$L_c$	Side of a cubical fragment
$L_{HE}$	Explosive Length
$L_W$	Length of fragments on warhead (equal to $L_{HE}$ in all cases)
$M_c$	Mass of a cubical fragment (also equivalent to $m_i$ )
$M_{HE}$	Mass of the explosive charge
$M_R$	Mass of a rod
$m_i$	Individual fragment mass
$M_{RC}$	Mass of a recovered cubical fragment
$M_T$	Total mass of fragments and liner on warhead
$N_{cc}$	Number of cubical fragments per column (along warhead length)
$N_c$	Number of columns of cubical fragments
$N_R$	Number of rods per warhead
$R$	Current warhead radius in computations
$R_b$	Radius of warhead at fragment separation in computations
$R_b/R_o$	Expansion ratio at fragment separation or breakage ratio; equivalent to $W_{RC}/L_c$
$R_o$	Initial inside radius of casing (metal fragments)
$W_{RC}$	Recovered cube dimension in the circumferential (hoop) direction.
$\alpha_f$	Azimuthal fragment-bearing sector angle
$\rho_f$	Fragment mass density

# DISTRIBUTION LIST

<u>No. of</u> <u>Copies</u>	<u>Organization</u>	<u>No. of</u> <u>Copies</u>	<u>Organization</u>
12	Commander Defense Documentation Center ATTN: DDC-TCA Cameron Station Alexandria, VA 22314	3	Commander US Army Missile Research and Development Command ATTN: DRDMI-R DRDMI-RFS DRDMI-RDP, H.W. Burnam Redstone Arsenal, AL 35809
1	Director Defense Advanced Research Projects Agency ATTN: Tech Info 1400 Wilson Boulevard Arlington, VA 22209	1	Commander US Army Tank Automotive Research & Development Command ATTN: DRDTA-RWL Warren, MI 48090
1	Commander US Army Materiel Development and Readiness Command ATTN: DRCDMA-ST 5001 Eisenhower Avenue Alexandria, VA 22333	2	Commander US Army Mobility Equipment Research & Development Command ATTN: Tech Docu Cen, Bldg. 315 DRSME-RZT Fort Belvoir, VA 22060
1	Commander US Army Materiel Development and Readiness Command ATTN: DRCDL 5001 Eisenhower Avenue Alexandria, VA 22333	1	Commander US Army Armament Materiel Readiness Command Rock Island, IL 61202
1	Commander US Army Aviation Research and Development Command ATTN: DRSAR-E 12th and Spruce Streets St. Louis, MO 63166	1	Commander US Army Armament Research and Development Command ATTN: DRSAR-CG Dover, NJ 07801
1	Director US Army Air Mobility Research and Development Laboratory Ames Research Center Moffett Field, CA 94035	5	Commander US Army Armament Research and Development Command ATTN: DRDAR-LC, Dr. J. Frasier DRDAR-LCA, Dr. E. G. Sharkoff Mr. L. Rosendorf Mr. G. Randers-Pehrson Mr. J. Pearson Dover, NJ 07801
2	Commander US Army Electronics Command ATTN: DRSEL-RD DRSEL-HL-CT, S. Crossman Fort Monmouth, NJ 07703		

# DISTRIBUTION LIST

<u>No. of Copies</u>	<u>Organization</u>	<u>No. of Copies</u>	<u>Organization</u>
3	Commander US Army Armament Research and Development Command ATTN: DRDAR-LCE, Dr. R. Walker DRDAR-TS-S DRDAR-LC, Mr. R. Nixon Dover, NJ 07801	1	HQDA (DAMA-MS) Washington, DC 20310
1	Commander US Army Heavy Diamond Labs ATTN: DRXDO-TI 2800 Powder Mill Road Adelphi, MD 20786	1	Commander US Army Research Office ATTN: Dr. E. Saibel P. O. Box 12211 Research Triangle Park NC 27709
2	Commander US Army Materials and Mechanics Research Center ATTN: J. Mescall D. Roylance Watertown, MA 02172	1	Commander US Naval Air Systems Command ATTN: AIR-604 Washington, DC 20360
1	Commander US Army Natick Research and Development Command ATTN: DRXRE, Dr. D. Sieling Natick, MA 01762	1	Commander US Naval Ordnance Systems Cmd ATTN: ORD-9132 Washington, DC 20360
1	Director US Army TRADOC Systems Analysis Activity ATTN: ATAA-SL (Tech Lib) White Sands Missile Range NM 88002	1	Chief of Naval Research ATTN: Code ONR 439, N. Perrone Washington, DC 20360
1	Deputy Assistant Secretary of the Army (R&D) Department of the Army Washington, DC 20310	1	Commander US Naval Air Development Ctr Johnsville Warminster, PA 18974
1	HQDA (DAMA-CSM) Washington, DC 20310	1	Commander US Naval Missile Center Point Mugu, CA 93041
1	HQDA (DAMA-ARP) Washington, DC 20310	2	Commander David W. Taylor Naval Ship Research & Development Center ATTN: D. R. Garrison A. Wilner Bethesda, MD 20034
		3	Commander US Naval Surface Weapons Center ATTN: Code TBB, D.W. Colbertson Mr. L. Hock Code TX, Dr. W.G. Soper Dahlgren, VA 22448

# DISTRIBUTION LIST

<u>No. of Copies</u>	<u>Organization</u>	<u>No. of Copies</u>	<u>Organization</u>
2	Commander US Naval Surface Weapons Center ATTN: WR-13 Tech Library Silver Spring, MD 20910	2	AFML Wright-Patterson AFB, OH 45433
6	Commander US Naval Weapons Center ATTN: J. Pearson, Code 383 J.S. Rinehart, Code 383 M. Backman, Code 3831 C.F. Austin, Code 3833 R.G.S. Sewell, Code 3835 J. Weeks, Code 3266 China Lake, CA 93555	1	AFFDL (FDT) Wright-Patterson AFB, OH 45433
2	Commander US Naval Research Laboratory ATTN: Tech Lib J. Baker Washington, DC 20375	3	ASD (YH/EX, John Rievley; XRHD, Gerald Bennett; ENYS, Matt Kolleck) Wright-Patterson AFB, OH 45433
1	Superintendent US Naval Postgraduate School ATTN: Dir of Lib Monterey, CA 93940	1	Headquarters National Aeronautics and Space Administration Washington, DC 20546
1	AFATL (Mr. Leonard T. Wilson) Eglin AFB, FL 32542	2	Director National Aeronautics and Space Administration John F. Kennedy Space Center ATTN: KN-ES-3 KN-ES-34 Kennedy Space Center, FL 32899
3	AFATL (DLRD, K. McArdle; DLRV, G. Crews; DLYD) Eglin AFB, FL 32542	2	Director National Aeronautics and Space Administration Langley Research Center ATTN: R. J. Hayduk Tech Lib Hampton, VA 23665
1	ADTC/DLJW (CPT D. Matuska) Eglin AFB, FL 32542	1	US Energy Research and Development Administration Los Alamos Scientific Lab ATTN: Mr. R. Craig, MS-960 Dr. L. Hantel, WX-2 Dr. Robert Karpp Los Alamos, NM 87544
1	AFATL (DLDL, MAJ J.E. Morgan) Eglin AFB, FL 32542		
2	AFWL (WLL) Kirtland AFB, NM 87117		
1	ASD (ASBRS) Wright-Patterson AFB, OH 45433		